JGR Solid Earth

RESEARCH ARTICLE
10.1029/2018JB017160

Lowermost Mantle Anisotropy Beneath Africa From Differential *SKS-SKKS* Shear-Wave Splitting

M. C. Reiss[1], **M. D. Long**[1], **and N. Creasy**[1]

[1]Department of Geology and Geophysics, Yale University, New Haven, CT, USA

Key Points:
- We present a comprehensive data set of discrepant *SKS-SKKS* splitting observations to infer lowermost mantle anisotropy beneath Africa
- Measurements suggest deformation at the border of the African large low shear velocity province and local changes in mantle flow geometry
- Within the large low shear velocity province, anisotropy is associated with an ultralow velocity zone, which may also feed the Afar plume

Supporting Information:
- Supporting Information S1
- Table S1

Correspondence to:
M. C. Reiss,
reiss@geophysik.uni-frankfurt.de

Citation:
Reiss, M. C., Long, M. D., & Creasy, N. (2019). Lowermost mantle anisotropy beneath Africa from differential *SKS-SKKS* shear-wave splitting. *Journal of Geophysical Research: Solid Earth*, *124*, 8540–8564. https://doi.org/10.1029/2018JB017160

Received 10 DEC 2018
Accepted 13 JUL 2019
Accepted article online 18 JUL 2019
Published online 14 AUG 2019

Abstract We investigate seismic anisotropy in the lowermost mantle in the vicinity of the African large low shear velocity province (LLSVP) using observations of differential *SKS-SKKS* shear-wave splitting. We use data from 375 permanent and temporary stations in Africa which enable us to map the spatial distribution of the anisotropic regions of the lowermost mantle in unprecedented detail. Our results corroborate previous findings that anisotropy is most clearly observed at the margins of the LLSVP, indicating strong deformation at its border, and they are generally consistent with a mostly isotropic LLSVP interior. We find that most discrepant *SKS-SKKS* measurements sample the lowermost mantle close to what is inferred to be the root of the Afar plume. We also identify strongly discrepant splitting in the vicinity of a previously mapped ultralow velocity zone (ULVZ) at the base of the LLSVP, beneath Central Africa. This represents an unusual observation of lowermost mantle anisotropy that is spatially coincident with a ULVZ and may reflect a unique anisotropic mechanism such as alignment of partial melt or the presence of strongly anisotropic magnesiowüstite. We interpret discrepant measurements outside of the LLSVP as likely reflecting a change in flow direction from the horizontal plane to a more vertical direction, which may be caused by deflection at the steep LLSVP border. We propose that our observations of D″ anisotropy associated with the African LLSVP can be explained by a mantle flow regime that maintains passive thermochemical piles with slab-driven flow and allows for the formation of upwellings at their edges.

1. Introduction

Understanding the patterns and drivers of Earth's mantle flow is a key challenge in deciphering major geodynamical processes such as subduction, orogenesis, and sea floor spreading. For more than 30 years, the role of the upper mantle in these processes has been very well studied using the seismic observation of shear-wave splitting (e.g., Long & Silver, 2009; Savage, 1999; Silver & Chan, 1991). This is caused by large-scale alignment of intrinsically anisotropic mantle minerals such as olivine or by layering or other alignment of isotropic velocity contrasts. Advances in geodynamical modeling and mineral physics have significantly increased our understanding of upper mantle flow, deformation, and shear-wave splitting (e.g., Becker et al., 2014; Karato et al., 2008). However, mantle flow patterns as well as deformation processes in the lower mantle, and their relationship to upper mantle processes, remain poorly understood. Accordingly, similar approaches to the study of upper mantle anisotropy have been used to study the lower mantle. As most of the mantle below the transition zone is seemingly isotropic (Meade et al., 1995), observations and modeling of seismic anisotropy resulting from flow and deformation are limited to the lowermost mantle, where the dominant minerals are thought to have significant single-crystal anisotropy and where deformation in the dislocation creep regime is plausible (for review see Nowacki et al., 2011).

The seismic structure of the Earth's lowermost mantle is characterized by two large areas in which seismic velocities (particularly shear velocities) are significantly lower than in the surrounding mantle (e.g., Lekic et al., 2012). These so-called large low shear velocity provinces (LLSVPs) are a robust feature observed in global tomographic models, though their small-scale details vary from model to model, and are located roughly antipodal to each other beneath Africa and the Pacific Ocean (Garnero et al., 2016). The edges of these LLSVPs are thought to be sharp and steeply dipping (Ni et al., 2002; Wang & Wen, 2007), while their interiors display significant heterogeneity, including small-scale features such as ultralow velocity zones (ULVZs; Garnero et al., 2016; Yu & Garnero, 2018). Spatial correlations have recently been noted between the occurrence of large igneous provinces and hot spot tracks, thought to be rooted in the deep mantle (Morgan, 1971), and the margins of the LLSVPs (Burke et al., 2008), although the nature of these correlations is under debate (Austermann et al., 2014). Additionally, areas

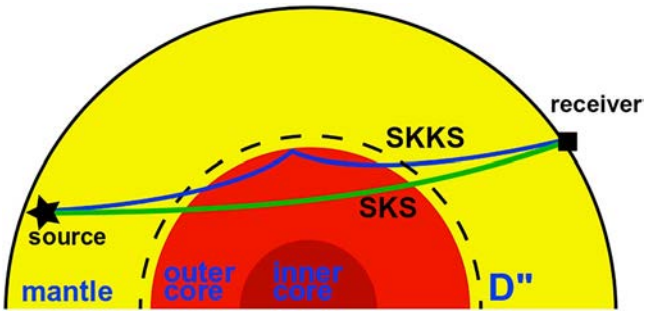

Figure 1. Sketch of raypaths used in this study. *SKS* and *SKKS* phases travel from a hypothetical earthquake source (star) to the receiver (rectangle).

of higher seismic velocity in the D″ layer at the base of the mantle correlate with expected locations of subducted slabs (Lithgow-Bertelloni & Richards, 1998).

Geodynamical studies focusing on understanding the origin of the LLSVPs and their associated mantle dynamics have led to three hypotheses: Either LLSVPs are purely thermal features or they are thermochemical in nature, with either a passive or active origin (Hernlund & McNamara, 2015). Early studies favored a purely thermal origin expressed as superplume or plume clusters in the mantle; given the strong heterogeneity and sharp velocity gradients at the margins of the LLSVPs, however, an additional compositional component is favored (e.g., Garnero et al., 2016; Hernlund & McNamara, 2015; and references in both). An active thermochemical origin proposes a global layer due to early Earth differentiation processes which over time leads to buoyancy-driven vertical flow (e.g., Davaille, 1999). A passive thermochemical origin postulates that LLSVPS are structures being created by slab remnants and are thus causally linked to the subduction cycle and surface tectonics (e.g., McNamara & Zhong, 2005).

Differentiation among these different hypotheses has important implications for our understanding of lower mantle structure, dynamics, and evolution, including the generation of plumes and the fate of remnant slabs. One promising avenue for increasing our understanding of lowermost mantle dynamics, and potentially for discriminating between active and passive models for LLSVP formation, is to map patterns of flow at the base of the mantle. Observations of shear-wave splitting due to lowermost mantle flow offer the possibility to study deformation and deduce flow patterns. Most studies of D″ anisotropy have applied shear-wave splitting analyses to pairs of seismic phases, such as *S-ScS* or *SKS-SKKS*, which have similar raypaths in the upper mantle but divergent raypaths in the lowermost mantle (e.g., Niu & Perez, 2004; Restivo & Helffrich, 2006; Lynner & Long, 2014; Ford et al., 2015; Creasy et al., 2017; see Figure 1). If differences in splitting behavior occur, they can be attributed to anisotropy in the D″ region. Making the link between anisotropy and flow patterns, however, is considerably more difficult than for the upper mantle. In particular, it is challenging to discriminate among different possible mechanisms for anisotropy, including shape-preferred orientation (SPO) of melt or compositional heterogeneities or crystallographic preferred orientation (CPO) of various candidate minerals. It remains unclear which mineral(s) might contribute to D″ anisotropy (e.g., Creasy et al., 2017; Nowacki et al., 2011). The likely main mineral constituents of the D″ layer are ~30% (Mg,Fe)O (ferropericlase) and ~70% (Mg,Fe)SiO_3, which may be present as bridgmanite in hotter regions and postperovskite in colder ones (Hirose et al., 2015). However, some workers have argued that postperovskite likely exists throughout the D″ layer (Koelemeijer et al., 2018).

In addition to the uncertainty regarding the dominant mineralogy, our understanding of single-crystal elasticity for candidate minerals, as well as their dominant slip systems under realistic pressures, temperatures, and strain rates, is currently hampered by experimental limitations (e.g., Nowacki et al., 2011; Yamazaki & Karato, 2013). It therefore remains difficult to confidently translate observations of seismic anisotropy to a unique deformation geometry; however, forward modeling studies are yielding some insights into plausible flow and anisotropy scenarios. For example, Tommasi et al. (2018) recently modeled anisotropy in D″ at lower mantle temperatures and pressures by predicting the CPO of postperovskite and ferropericlase for flow parallel to the core-mantle boundary (CMB) and for changes in the flow direction associated with both upwelling and downwelling. Results indicate that the polarization of fast shear waves is often subparallel to the flow direction, but this relationship breaks down in proximity to changes in the flow pattern; in this case, shear-wave splitting varies strongly as a function of backazimuth.

Anisotropy in the lowermost mantle beneath Africa has been consistently observed at the margins of the LLSVP (Cottaar & Romanowicz, 2013; Lynner & Long, 2014; Wang & Wen, 2004), with most measurements suggesting anisotropy just outside of the LLSVP (Cottaar & Romanowicz, 2013; Ford et al., 2015). The interior of the African LLSVP generally seems to be isotropic or nearly so, although Wang and Wen (2004) identified the presence of anisotropy within the southern part of the LLSVP. Later work by Lynner and Long (2014), who examined the same region, found anisotropy located at the eastern margin of the LLSVP, with little or no splitting for paths sampling within the LLSVP itself. Ford et al. (2015) found robust evidence for strong

anisotropy at the eastern margin of the African LLSVP close to the Afar plume; forward modeling of their observations suggested CPO of postperovskite with the [100] crystallographic axis oriented nearly vertically, implying vertical flow. Cottaar and Romanowicz (2013) observed a change of anisotropy from strong (outside the LLSVP) to weak (close to the margin) and absent (inside the LLSVP) at the southern edge of the LLSVP, which they explain by changes in flow from horizontal to vertical. All of these studies, however, have been limited in their spatial coverage of the African LLSVP as a whole.

Here we present a large and comprehensive data set of *SKS-SKKS* splitting discrepancy measurements that sample the lower mantle beneath Africa, with the goal of characterizing the spatial variability in lowermost mantle anisotropy in and around the African LLSVP as fully as possible. Our work builds on previous studies of *SKS-SKKS* splitting discrepancies beneath Africa by Wang and Wen (2004) and Lynner and Long (2014) in three important ways. First, as in Lynner and Long (2014) but in contrast to Wang and Wen (2004), we focus on *SK*(*K*)*S* phases from the same seismograms (i.e., the same event-station pairs), because in this case the argument that discrepancies suggest a contribution to splitting from the lowermost mantle is more straightforward. Second, we extend the coverage of these previous studies in both space and time by including a much larger set of stations (Figure 2) and including data from 1990 to the present. Third, we implement two different measurement methods in order to provide the most robust identification possible of discrepant splitting. Specifically, we use both the standard transverse energy minimization method of Silver and Chan (1991) and the splitting intensity method of Chevrot (2000). The latter method has recently been applied to study lowermost mantle anisotropy at the edge of the Pacific LLSVP (Deng et al., 2017) and provides a robust strategy for discriminating discrepant splitting with high confidence. These improvements enable us to present a large, comprehensive data set of *SKS-SKKS* splitting discrepancy measurements, allowing us to map the spatial distribution of anisotropy at the base of the mantle beneath Africa in unprecedented detail.

2. Data and Methods

2.1. Shear-Wave Splitting Methodology

When a polarized shear wave travels through an anisotropic medium, it is split into fast and slow wave components that are orthogonally polarized. The delay time between the two wave trains can be used to infer the strength and/or thickness of the anisotropic layer (e.g., Savage, 1999). There are several methods to measure shear-wave splitting (see Long & Silver, 2009, for a review); in this study we apply transverse energy minimization (Silver & Chan, 1991) and splitting intensity (Chevrot, 2000). For both, we use the initial polarization of the shear wave to rotate the horizontal seismogram components into the radial/transverse coordinate system. For core-refracted shear waves, the initial polarization corresponds to the backazimuth, as shear waves become radially polarized (i.e., in the source-receiver plane) upon leaving the CMB. After the transformation, a time window is selected around the teleseismic *SK*(*K*)*S* phase. The transverse minimization method then employs a grid search over possible values of the two splitting parameters, namely, φ (fast polarization direction) and δt (delay time). The pair which best reduces the energy on the original transverse component after the waveforms are rotated and time-shifted to account for the effect of splitting is taken as the best estimate of the splitting parameters. The splitting intensity (*SI*), as defined by Chevrot (2000), is the amplitude of the transverse component relative to the time derivative of the radial component; we calculate this quantity by projecting the transverse component onto the radial component's time derivative:

$$SI = -2\,\frac{T(t)R'(t)}{\left|\left|R'(t)\right|\right|^2},$$

where $T(t)$ is the transverse component, $R'(t)$ the time derivative of the radial component, and $||R'(t)||^2$ the squared norm of $R'(t)$. We estimate 95% confidence levels from the mean square error given by Appendix B of Chevrot (2000). The splitting intensity relates to the splitting parameters φ and δt by

$$SI \approx -\frac{1}{2}\,\delta t \sin 2\beta$$

where β is the angle between the backazimuth and the fast polarization direction φ. As discussed in detail by Deng et al. (2017), the splitting intensity has some important advantages over the transverse energy minimization method for *SKS-SKKS* splitting discrepancy studies. Individual splitting intensity

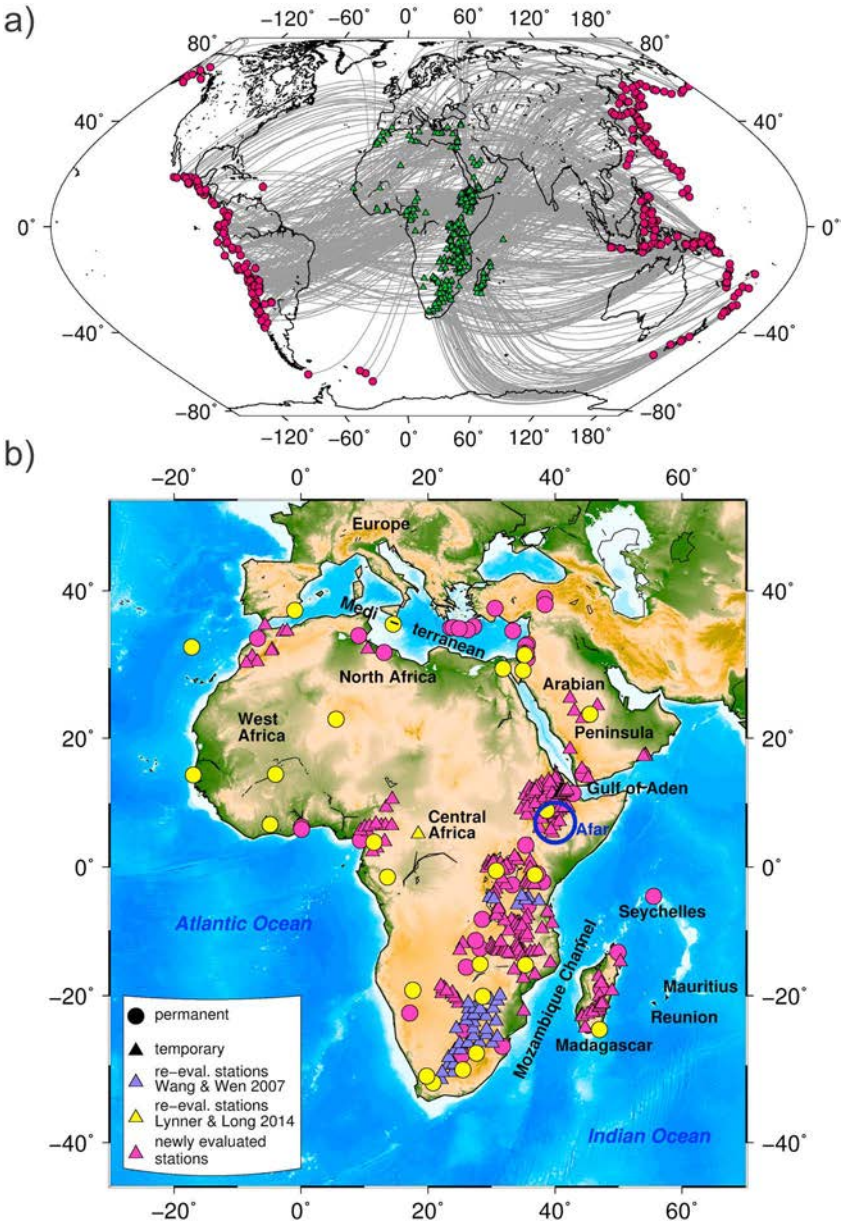

Figure 2. (a) Raypaths for all station-event pairs used in this study. Earthquakes are denoted by magenta circles, and stations are shown with green triangles. Raypaths between stations and earthquakes are solid gray lines. (b) Topographic map of Africa and surrounding region with names of geographic locations. Stations used in this study are denoted by triangles and color coded to show which stations were examined by earlier studies. Magenta triangles show stations only used in this study, while yellow and purple triangles denote stations used by Lynner and Long (2014) and Wang and Wen (2007), respectively.

measurements are more robust than traditional methods (e.g., Monteiller & Chevrot, 2010), and differences in splitting for *SKS* and *SKKS* phases can be expressed in a straightforward way via splitting intensity differences (Deng et al., 2017).

We carried out our analysis using the SplitRacer package of Reiss and Rümpker (2017), which in its original form only implemented the transverse energy minimization method. For this study, we incorporated splitting intensity measurements into the code, following Deng et al. (2017). We calculated 95% confidence intervals for all parameters based on the *F* test (Silver & Chan, 1991), with an adjustment for the number of degrees of freedom given by the equations of Walsh et al. (2013), who showed that the original error estimates in Silver and Chan (1991) were too low.

2.2. Data Selection and Processing

To build our shear-wave splitting discrepancy database, we identified both permanent broadband stations and temporary deployments from 1990 onward in Africa and adjacent areas. We used data for 166 stations from five individual networks obtained from the GEOFON data center and 877 stations from 36 networks hosted by the Incorporated Research Institutions for Seismology Data Services, for a total of 1,043 stations. (For comparison, Long and Lynner, 2014, used data from 34 permanent stations, while Wang & Wen, 2004, used 119 permanent and temporary stations.) We requested waveforms for these stations for events with $M >$ 5.8 at an epicentral distance range between 108° and 122°, over which both *SKS* and *SKKS* phases are commonly visible (Niu & Perez, 2004). We ultimately downloaded and processed over 90,000 waveforms.

Our processing routine, applied identically for every event-station pair, incorporated the following steps. After data download, we applied a band-pass filter with corner periods at 6 and 25 s and used a signal-to-noise cutoff ratio of 1.5 to automatically select usable *SKS-SKKS* pairs, using the initial processing routine implemented in SplitRacer. Events were retained for visual inspection if both phases were above the chosen signal-to-noise ratio threshold, which was chosen conservatively in order to retain data at noisy stations. We then visually inspected all phases and manually altered the time window around the phase for the shear-wave splitting analysis if necessary. We discarded events which did not have clear arrivals for both *SKS* and *SKKS*. We used a long-period filter on the particle motion of the phase to determine any sensor misalignments (Reiss & Rümpker, 2017; see also Hanna & Long, 2012). For every station, we used a mean misalignment value, derived from all high-quality *SK(K)S* waveforms at the station, to correct for misalignment. Some stations displayed misalignment changes over time, for which we corrected accordingly.

We then rotated the north/east components of each phase to radial/transverse and simultaneously applied both measurement methods. Examples of high-quality measurements for three sample *SKS-SKKS* pairs are shown in Figure 3. We did not rely on a single, arbitrarily chosen time window; instead, we calculated splitting parameters for 50 random windows around the original window selection. This ensures that the measurement is statistically robust (Reiss & Rümpker, 2017; Teanby et al., 2004). For each measurement, we checked that the estimated splitting parameters φ and δt minimize the energy of the transverse component by visually confirming that the particle motion was corrected after the application of the inverse splitting operator (see Figure 3, second column). We also visually inspected the transverse component waveforms, to confirm that they resembled the time derivative of the radial component. A further quality control step was provided by checking whether the splitting parameters varied over the 50 used time windows in the histogram (Figure 3, third column); only phases that had stable measurements over all time windows were kept. Finally, we required that the mean 95% confidence levels from all time windows had to be well defined. We derive our final error estimates by stacking all 95% confidence levels from 50 time windows and calculating a mean.

A measurement was characterized as a null measurement when the energy on the transverse component was nonexistent (more specifically, not above the transverse component noise level) and the particle motion was linear before the application of the inverse splitting operator. For our final data set, we retained measurement pairs for which both the *SKS* and *SKKS* phases displayed clear splitting or were null. Splitting measurements were divided into three quality categories defined by their confidence interval. The best category has a φ error interval of <30° and a δt error interval of <0.75 s on both measurements. The good category includes measurements which have a φ error interval of <60° and a δt error interval of <1.5 s. Very few measurements (30) of phases were kept with larger errors (and only if the other phase's measurement is in the best category; see Table S1 in the supporting information for details). We note that our error estimates for the transverse component minimization measurements may be slightly larger than in other studies, due to our usage of the Walsh et al. (2013) degree-of-freedom formulation as well as the 95% confidence level stacking procedure.

3. Results

Our final set of *SKS-SKKS* splitting discrepancy measurements consisted of 896 *SKS-SKKS* pairs, recorded at 375 individual stations (from 33 individual networks), from 346 individual events. Raypaths for each of these 896 station-event pairs are shown in Figure 2. Compared to the total number of waveforms examined in this study, 896 pairs seems like a small number, but this yield is comparable to other studies of *SKS-SKKS*

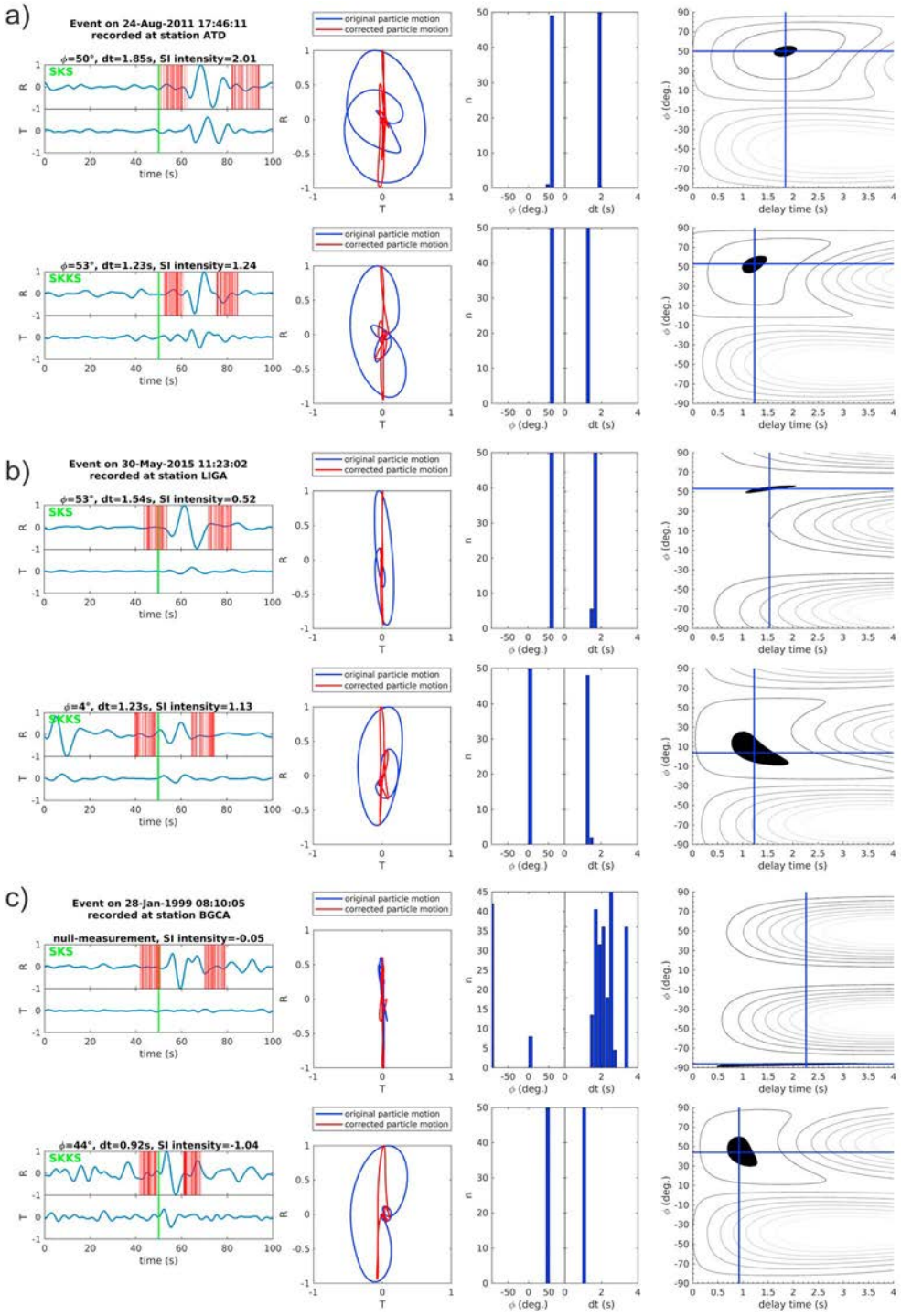

Figure 3. Discrepant *SKS-SKKS* shear-wave splitting data examples, measured at three different stations. The first column shows 100 s of the band-pass-filtered (6–25 s) radial and transverse components for the phase in question (*SKS* or *SKKS*, denoted in green letters; the theoretical arrival time is marked with a green line). The red lines denote the 50 time windows used in the analysis. The estimated shear-wave splitting parameters and splitting intensity measurements are shown above the radial component. In the second column, the original (uncorrected) particle motion for the initially chosen time window is shown in blue, with the corrected particle motion in red. The third column shows a histogram of estimated φ and dt values for the 50 time windows. The last column shows the 95% confidence level atop the transverse component energy grid, with the best-fitting splitting parameters marked with a blue cross. (a) Example of an event on 24 August 2011 recorded at station ATD with a backazimuth of 268°. This is a permanent station of the Geoscope network and is located in the Republic of Djibouti. (b) Example of an event on 30 May 2015 recorded by station LIGA with a backazimuth of 64°. This station was part of the temporary experiment Study of Extension and Magmatism in Malawi and Tanzania (network code YQ). (c) Example of an event on 28 January 1999 recorded at station BGCA with a backazimuth of 5°. This station belonged to the Global Telemetered Seismograph Network (GT) until mid-2002.

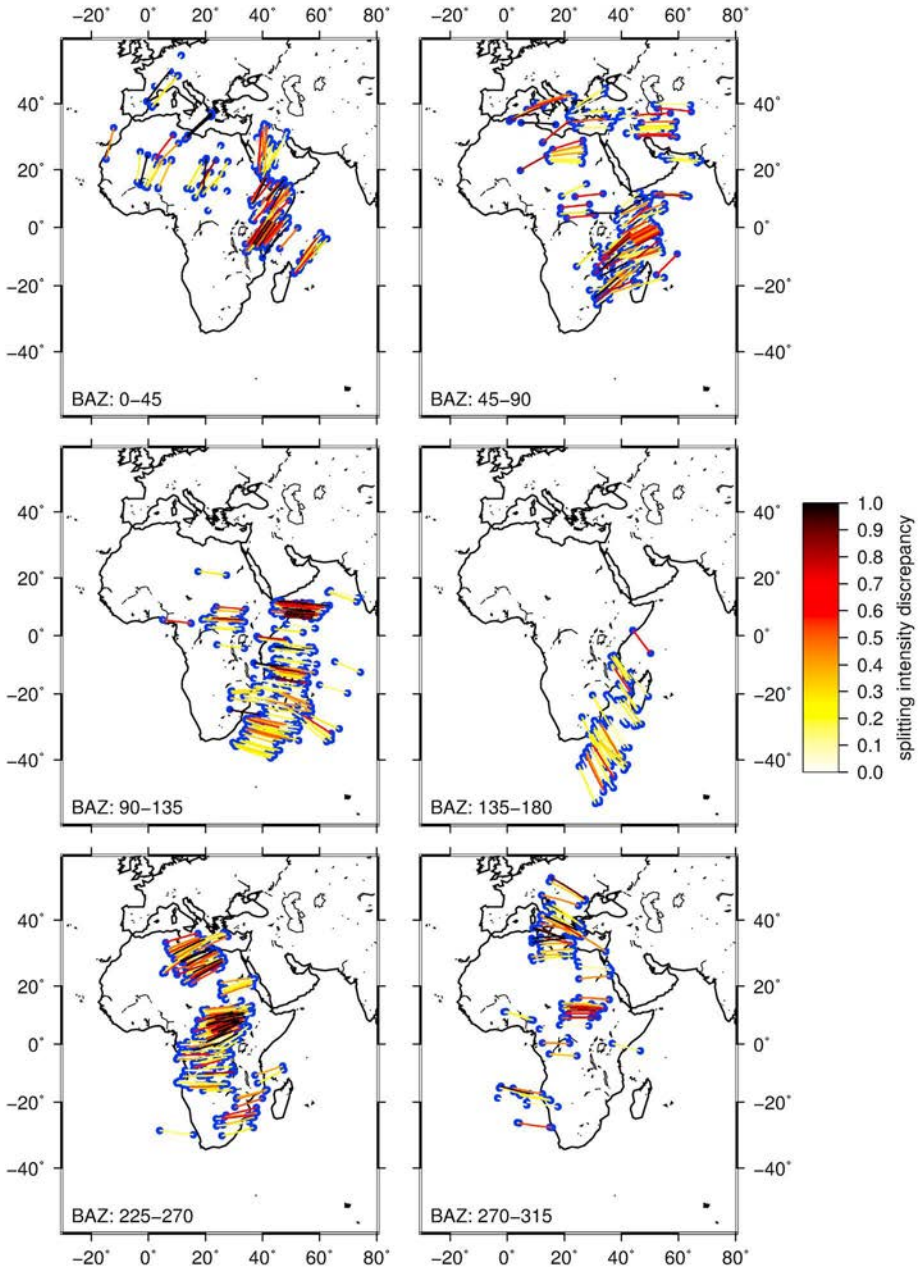

Figure 4. Splitting discrepancy results, binned by backazimuth (bin size 45°) in order to show details. For each event-station pair, we calculated the pierce points of the *SKS* and *SKKS* phase atop the D″ layer at a depth of 2,641 km (blue circles). The connecting line between the pierce points of each event's *SKS* and *SKKS* phases is colored by the difference in their splitting intensity, as shown in the color bar to the right. We exclude the 180–225° and 315–360° backazimuthal bins from this figure, as they have very few measurements. The color bar is saturated at a splitting intensity discrepancy of 1 for better visibility.

splitting discrepancies (e.g., Long, 2009; Lynner & Long, 2014; Deng et al., 2017). Because most of the data we use came from temporary deployments (with typical run times between 1 and 3 years), we found that for a given station, it was often impossible to find even one event for which both *SKS* and *SKKS* phases were clearly recorded and had stable splitting measurements.

Our *SKS-SKKS* splitting discrepancy results are shown in Figure 4. In this view, we choose to display splitting intensity discrepancies (i.e., the difference in measured splitting intensity value between the phases) rather than splitting parameters φ and δt, as this plotting convention results in simpler maps for the large amount

Table 1
Overview of Measurements per 45° Backazimuth Bin

Bin	No. of pairs	Percentage of data set
0–45°	113	12.6
45–90°	182	20.3
90–135°	202	22.5
135–180°	58	6.5
180–225°	4	0.5
225–270°	258	28.8
270–315°	75	8.4
315–360°	4	0.5

of data. Figure 4 displays our measurements binned by backazimuth (bin size of 45°) for better visibility and to highlight spatial variations among groups of measurements with similar raypaths. As demonstrated by Figure 4, the backazimuthal coverage of our data set is good but not uniform. The data set is strongly dominated by events from Central to South America, as well as the western subduction zones of the Pacific plate. We note that the two backazimuthal bins of 180–225° and 315–360° are nearly empty and are not portrayed in Figure 4 (see Table 1 for comparison).

In the 0°–45° bin, highly discrepant measurements cluster in the region beneath the Gulf of Aden and along the eastern African shoreline, while nondiscrepant measurements sample the region beneath Central to North and West Africa. The second bin also shows strongly discrepant measurements along the eastern African coast, further to the south, and highly discrepant splitting toward the Indian Ocean north of Madagascar. Single (non)discrepant measurements are scattered throughout northern Africa, the Arabian Peninsula, and Mediterranean with a small cluster of nondiscrepant measurements beneath North Africa. Events in the 90–135° bin exhibit a cluster of strongly discrepant measurements that sample to the south of the Arabian Peninsula, close to the inferred location of the Afar plume. Beneath the Mozambique Channel between Africa and Madagascar, we observe mostly nondiscrepant pairs, with scattered moderately discrepant measurements. This trend continues in the 135–180° bin, which exhibits mostly nondiscrepant measurements to the south and southwest of Africa. The fifth bin, which includes ~30% of the measurements (dominated by seismicity in Central and South America), shows strongly discrepant measurements that sample beneath Central Africa and beneath North Africa toward the Mediterranean. A mix of discrepant and nondiscrepant samples to the south of this group, with some clustering of moderately discrepant events sampling beneath the southeastern coastline of Africa. The final bin includes another cluster of strongly discrepant measurements beneath Central Africa, with a mix of nondiscrepant and discrepant measurements sampling beneath the Mediterranean into southern Europe.

In order to interpret our results, it is necessary to carefully consider how our data set as a whole is distributed spatially, as well as how discrepant pairs are distributed. Figure 5 shows the spatial distribution of our data set's sampling in the lower mantle, calculated via a data density measure. For each *SKS-SKKS* pair, we use the calculated pierce points through the top of the D″ layer and discretize a line with 20 points between them. Given that the pierce points projected onto the surface are approximately 10° apart, this means there are roughly two points per degree. We then initialized a grid of 5° × 5° cells and populated the grid cells with the discretized lines. The results are shown in Figure 5, initially for the entire data set (Figure 5a), which shows how many discretized line points lie in each grid cell. Figure 5a demonstrates that our data coverage is strongest in northern and Central Africa, as well as Gulf of Aden and along the eastern coastline. In order to visualize how the average splitting intensity discrepancy varies over our study area, we repeated the same procedure but allocated the observed splitting intensity discrepancy (whether small or large) to each discretized line point. For each 5° × 5° cell, we calculated a mean splitting intensity; results are shown in Figure 5b. This method of visualizing the data shows that strongly discrepant grid cells are distributed throughout our study region, with clusters beneath northwest Africa into the Mediterranean and Europe, and beneath southwest Africa to east of Madagascar. Grid cells with low average splitting intensity discrepancy values cluster beneath south to southwest Africa and northeast Africa across the Mediterranean into Europe. Many nondiscrepant cells lie at the edges of our study region.

In order to highlight regions with good data sampling and eliminate regions that appear discrepant but that are poorly sampled, we repeated this exercise but removed all grid cells with fewer than 40 data points, which corresponds to roughly four measurements per degree. These results are shown in Figures 5c and 5d, which represent our results for areas of good data coverage. A comparison between Figures 5d and 5b illustrates which regions of our study area exhibit robust (and thus interpretable) splitting discrepancies. Areas that exhibit both good data coverage and significantly discrepant splitting include regions beneath northern and Central Africa, as well as beneath the Gulf of Aden and along the eastern African coastline.

Areas with good data coverage but nondiscrepant (or only weakly discrepant) splitting include the lowermost mantle beneath southeast and northeast Africa.

4. Interpretation of Splitting Discrepancies

4.1. Upper Mantle Contributions: Possible Effects

A key question in any study that uses *SK*(*K*)*S* phases to probe lowermost mantle anisotropy is to what extent the individual measurements reflect a contribution to splitting from the upper mantle. It is well known that upper mantle anisotropy makes the primary contribution to *SK*(*K*)*S* splitting worldwide (e.g, Becker et al., 2012), and contributions from the lower mantle are a second-order effect. Some *SK*(*K*)*S* studies of lower mantle anisotropy explicitly correct waveforms for the effect of splitting due to upper mantle anisotropy and attribute the remaining signal to the lowermost mantle (examples include Long & Lynner, 2015; Ford et al., 2015; and Creasy et al., 2017; Lynner & Long, 2014, also carried out upper mantle corrections for a small subset of their stations). We now consider the nature of likely contributions from upper mantle anisotropy to our data set, as this informs our strategy for the interpretation of our *SKS-SKKS* data set.

Many (~60%) of the stations used in this study are located in the East African Rift. Previous shear-wave splitting studies in this region (Homuth et al., 2014; Gao et al., 2010; Bagley & Nyblade, 2013; Tepp et al., 2018) have shown that apparent splitting varies strongly both spatially and with backazimuth. This leads to the conclusion that anisotropy in the upper mantle beneath the East African Rift is highly complex, with strong lateral variation and multiple layers of anisotropy. Possible candidate mechanisms for upper mantle anisotropy include partial melt beneath the rift system (aligned via SPO), as well as asthenospheric flow, perhaps driven by the African superplume. In adjacent regions of the Indian Ocean, Seychelles, La Reunion, and Madagascar, stations often display similarly complex splitting parameters that likely reflect complex upper mantle anisotropy (Barruol & Fontaine, 2013; Hammond et al., 2005; Reiss et al., 2016). Upper mantle anisotropy beneath these regions may be caused by a combination of plate- and/or density-driven asthenospheric flow and interactions with localized plumes, with a possible fossil anisotropy component in the mantle lithosphere beneath continental Madagascar. Beneath northern Africa, shear-wave splitting measurements have been found to be consistent with one anisotropic layer in the upper mantle, indicative of northward movement of the African plate and flow deflected at the root of the African plate (Lemnifi et al., 2015). Taken together, these previous studies show that for most of the data used in this study (with the possible exception of stations located in northern Africa), the upper mantle contribution to *SK*(*K*)*S* splitting is likely to be complex and vary strongly with backazimuth.

Furthermore, for many of the temporary stations we used, the backazimuthal coverage is too poor to reliably identify likely vertical and/or horizontal variability in upper mantle anisotropy, again implying that we cannot confidently correct for the influence of the upper mantle. Most of the permanent stations we used have better azimuthal coverage, but again many have also been found to display complex patterns of upper mantle anisotropy (e.g., Barruol & Hoffmann, 1999), for which we cannot easily account in our analysis. Because of this likely complexity throughout our study region, we do not attempt to correct our measured splitting parameters for the effect of upper mantle anisotropy, as has been done in some previous studies. Instead, we focus our interpretation on discrepancies between pairs of phases, as reflected in measurements made with the splitting intensity method (following Deng et al., 2017). Because of the similarity in *SKS* and *SKKS* raypaths in the upper mantle (Figure 1), we can assume that both phases accumulate a similar contribution to the total splitting intensity from upper mantle anisotropy. Significant discrepancies between phase pairs thus indicate a contribution from lowermost mantle anisotropy to one or both phases, with a different contribution from D″ anisotropy to *SKS* versus *SKKS*. The splitting intensity is a particularly convenient quantity to work with for *SKS-SKKS* discrepancy measurements (Deng et al., 2017), because it is a commutative quantity that represents a straightforward sum of the contribution of multiple anisotropic layers (Chevrot, 2000; Silver & Long, 2011).

Niu and Perez (2004) showed that in general, pronounced differences in shear-wave splitting between *SKS* and *SKKS* phases are due to anisotropy in the lower mantle. Before we can interpret our splitting intensity discrepancy data set in detail, however, we first consider to what extent effects other than lower mantle anisotropy may contribute to the observed discrepancies, such as full waveform interference effects or heterogeneous anisotropic structure in the shallow upper mantle or crust (Deng et al., 2017). Lin et al. (2014)

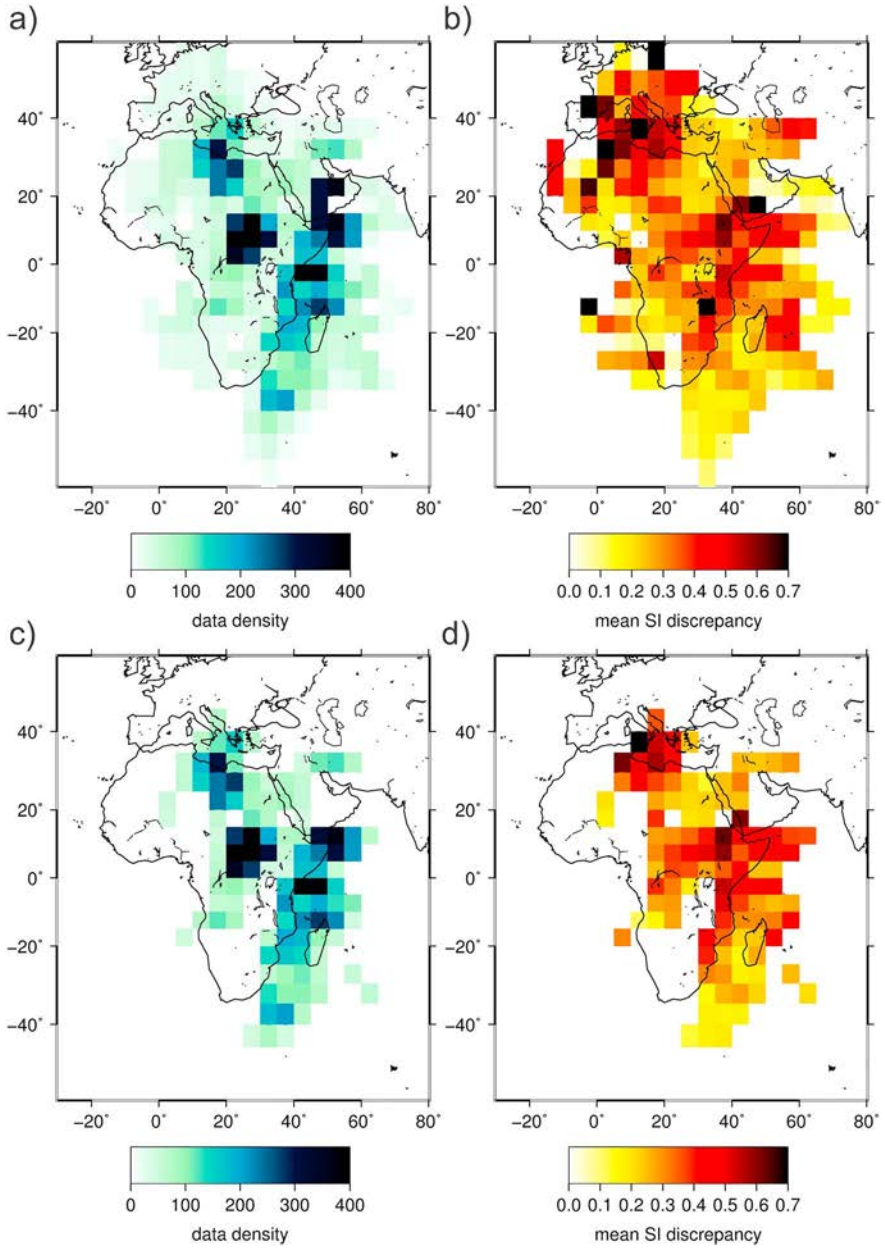

Figure 5. Measurement density plots showing the spatial coverage of our data set and the spatial variability in mean splitting intensity discrepancy. Connecting lines between pierce points of every *SKS-SKKS* pair are discretized onto a 5° grid. (a) Number of line points in each grid bin. (b) Average splitting intensity discrepancy per grid bin. (c) Number of line points per grid bin for every bin that hosts a minimum of 40 points. (d) Average splitting intensity discrepancy per grid bin for every bin that hosts a minimum of 40 points. For comparison, all color maps are saturated. The color bar in (a) and (c) is fixed at 400 per grid, and the color bar in (b) and (d) is fixed at 0.7 to emphasize the content of every grid bin. In (a) 14% of the data are above the saturation point, and in (c) 16% of the data are above the saturation point. Maximum value for the splitting discrepancy is 1.1 in (b) and 0.9 in (c).

showed that for a homogenous upper mantle, finite frequency wave propagation effects may contribute up 0.2 splitting intensity discrepancy between *SKS-SKKS* pairs due to waveform interferences. They further found that splitting intensity measurements are strongly affected by shallow sources (<20 km) with distances less than <100°, while waveform interference is strongest at event distances ~130°. In our study, we use events of epicentral distances from 108° to 122°, which helps to rule out strong contributions of finite frequency wave propagation effects on our splitting intensity measurements.

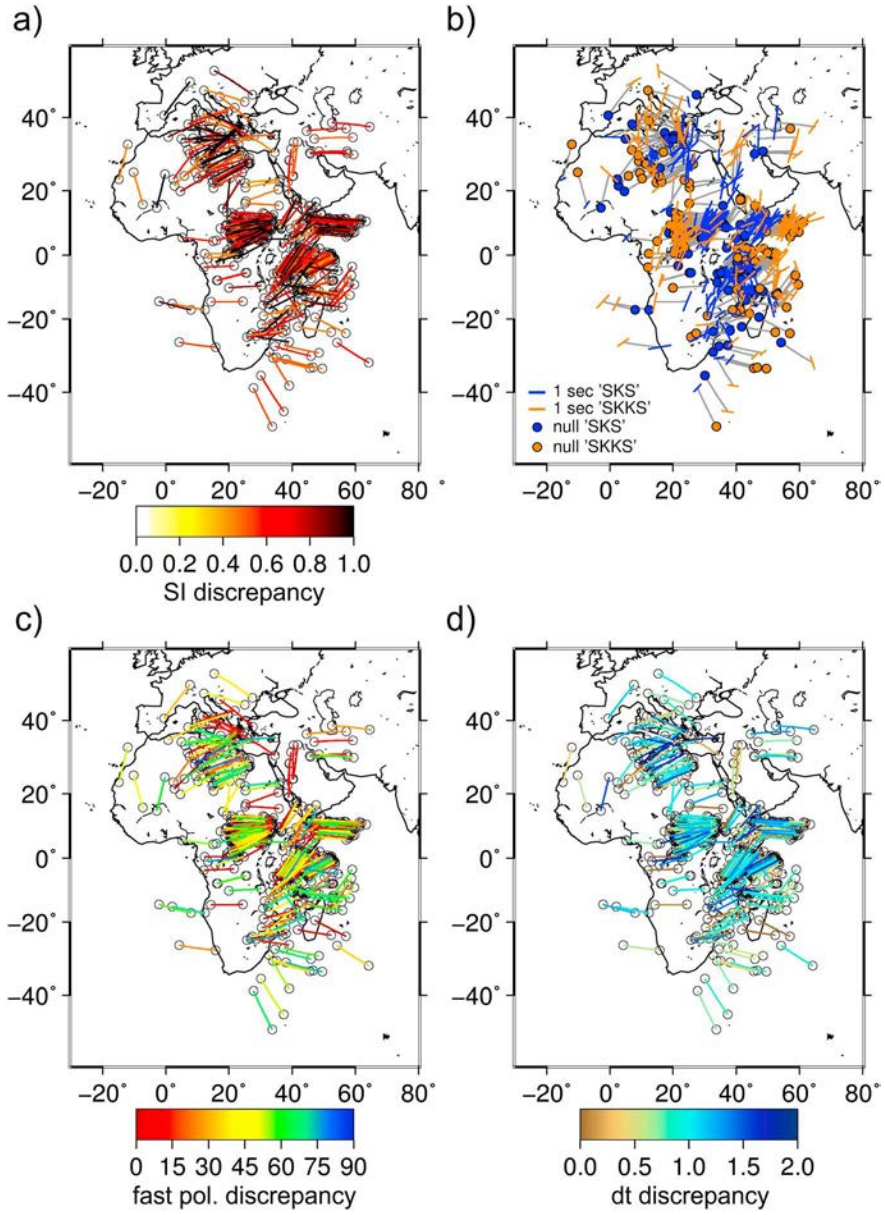

Figure 6. Map of highly discrepant *SKS-SKKS* pairs, based upon a threshold difference in splitting intensity measurements of 0.4. (a) Map of splitting intensity discrepancies. Pierce points for each phase are plotted as black circles and connected by lines whose color corresponds to the difference in splitting intensity between the phases, as shown by the color bar at the bottom. (b) Map of splitting parameters for each discrepant pair. Splitting results are plotted at the rays' pierce points at the top of the D″, with *SKS* phases in blue and *SKKS* phases in orange. The length of each bar is scaled by the delay time, while its orientation corresponds to the fast polarization direction. Null measurements are denoted by circles. Corresponding phases of each pair are connected by thin gray lines. (c) Map of fast polarization direction discrepancies, with the color bar indicating the magnitude of the discrepancy (degrees) as indicated. (d) Map of delay time discrepancies, with the color bar indicating difference in delay times (s).

Next, we examine the possible influence of shallow anisotropic heterogeneity (crust or upper mantle) on our splitting intensity measurements. We calculated pierce points for every *SKS-SKKS* pair at 100 and 200 km depth in the mantle and found that the average distance between the pierce points is 12 km at 100 km depth and 23 km at 200 km depth for our data set. At a depth of 200 km, Fresnel zone estimates from finite difference waveform modeling for a phase pulse of an 8 s period suggest a lateral sensitivity of ~140 km, and for a 16 s period phase pulse, a sensitivity of ~220 km (Rümpker & Ryberg, 2000). At a depth of 100 km, Fresnel zones estimates provide a lateral sensitivity of 110 km for a pulse of 8 s and 180 km for a pulse of 16 s (Rümpker & Ryberg, 2000). The

average observed characteristic period for *SK(K)S* arrivals in our data set is ~12 s. This means that even for shallow heterogeneous anisotropy, Fresnel zones between *SKS* and *SKKS* overlap significantly in the upper mantle and essentially sample the same region. While there is less overlap in sensitivity at shallower depth (i.e., within the crust), unrealistically strong crustal anisotropy would be required to explain strong discrepancies in splitting (see also Lynner & Long, 2012); furthermore, heterogeneous crustal anisotropy beneath individual stations cannot explain the generally consistent regional patterns evident in Figure 4.

4.2. Lowermost Mantle Anisotropy Inferred From Splitting Intensity Discrepancies

Based on the arguments in section 4.1, for the purpose of our study we define significantly discrepant pairs to have a splitting intensity difference of at least 0.4. This cutoff allows for modest contributions to discrepant splitting from finite frequency wave propagation effects and/or shallow anisotropic heterogeneity (also see Deng et al., 2017); we only interpret discrepancies of 0.4 and greater as requiring a contribution from the lowermost mantle. Under this definition, 306 of the 896 *SKS-SKKS* pairs in our data set are significantly discrepant. Of these, a very small number (five pairs out of 306) have overlapping error bars on the splitting intensity estimates; for the remainder (roughly one third of the data), we can make a clear argument that a contribution from lower mantle anisotropy is required. Using this definition of a significantly discrepant measurement, we show the geographic distribution of the 301 discrepant pairs in Figure 6; we show both the splitting intensity differences (Figure 6a) and the corresponding splitting parameters (φ and δt) for each phase (Figure 6b). Additionally, Figures 6c and 6d show the discrepancies of the fast polarization and delay time between *SKS* and *SKKS* phases, respectively.

Interestingly, the fraction of discrepant pairs in our data set (~33%) is significantly higher than that found by Niu and Perez (2004) in their global data set; they found that only 5% of *SKS-SKKS* pairs are discrepant globally. Lynner and Long (2014), who examined a set of stations with significant overlap with our study, found ~15% discrepant pairs based on discrepancies of the splitting parameters φ and δt. A large part of the difference between our study and that of Niu and Perez (2004) is likely due to our study's regional focus on the lowermost mantle beneath Africa. However, we attribute at least some of this difference in the fraction of discrepant pairs to our usage of the splitting intensity method, which effectively combines both splitting parameters φ and δt in one expression and thus reduces the problem of defining discrepancies to one (robust and straightforward) variable. Additionally, we applied very strict criteria to our *SKS-SKKS* pairs based on stringent quality control requirements on both methods as described above. This may have effectively limited the number of measurements; we speculate that it likely led to the elimination of many noisy null-null (nondiscrepant) pairs. Our finding that a relatively large fraction of *SK(K)S* phases may be affected by lowermost mantle anisotropy, at least beneath Africa, speaks to the ongoing debate over whether *SK(K)S* phases sample D″ effectively (see, e.g., Tommasi et al., 2018).

As in other *SKS-SKKS* discrepancy studies, we also observe a considerable amount of scatter of individual nondiscrepant and discrepant measurements with similar raypaths (Lynner & Long, 2014; Deng et al., 2017). However, a comparison between Figure 4, which shows the entire *SKS-SKKS* data set, and Figure 5, which shows our measurement density as well as mean splitting intensity values per grid point, demonstrates that despite the scatter, there are clear and convincing spatial patterns. Specifically, our observations demonstrate that there are areas with good data coverage where discrepant measurements dominate (i.e., central and northern Africa) and other areas with good data coverage where nondiscrepant measurements prevail (i.e., south of Africa). Thus, even though individual measurements show considerable scatter, spatial patterns in our data set are robust and show distinct areas dominated by discrepant versus nondiscrepant measurements.

An intriguing aspect of our data set is that there are regions sampled by rays propagating at multiple backazimuths that display a clear dependence of splitting intensity discrepancy values on backazimuth. This is evident for the region beneath the Mozambique Channel, where events from the 45–90° bin display discrepant measurements, while events from the 90–135° and 135–180° bins are generally nondiscrepant (Figure 4). This is also true beneath northern Africa, where events from the 45–90° bin are mostly nondiscrepant, but *SKS-SKKS* pairs are strongly discrepant in the 225–270° bin. We explore this further by examining the shear-wave splitting parameters (φ and δt) per 45° backazimuth (as in Figure 4) for discrepant measurements (as defined by differences in splitting intensity of 0.4 and larger). As shown in Figure 7, many highly discrepant measurements are associated with *SKS-SKKS* pairs exhibiting one null and one split measurement, with most null measurements corresponding to *SKKS* phases. This is particularly pronounced beneath the Mozambique

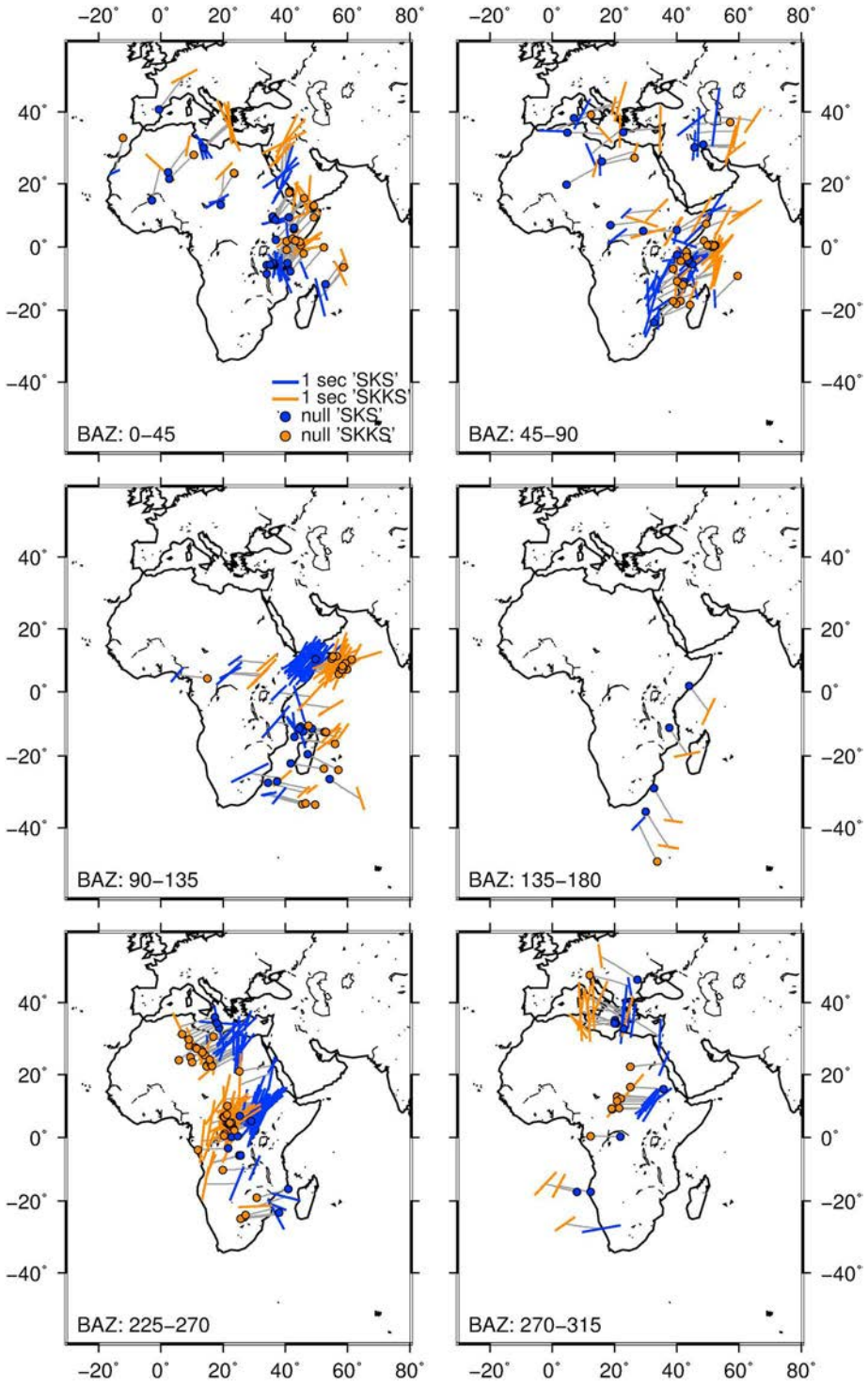

Figure 7. Shear-wave splitting parameters (φ and δt) for strongly discrepant *SKS-SKKS* pairs (as defined via the splitting intensity difference) in 45° backazimuth bins. We plot individual results of each *SKS* and *SKKS* phase on pierce points at the top of D″. *SKS* phases are shown in blue, while *SKKS* phases are shown in orange. The length of each bar is scaled by the delay time, while its orientation (angle from north) denotes the fast polarization direction. Null measurements are denoted with circles. *SKS-SKKS* pairs are connected by gray lines.

Channel (45–90° bin) and beneath central and northern Africa (225–270°). We therefore infer that anisotropy in the D″ layer beneath this area must have a significant amount of azimuthal variability, with strong dependence of the initial polarization or backazimuth (Ford et al., 2015; Nowacki et al., 2011).

There are also clusters where significant splitting intensity discrepancies result from two split phases, such as in the Mediterranean (0–45° and 270–315° bins) and areas where clusters of split-null and split-split phases coexist (i.e., Gulf of Aden, 90–135° bin). As we did not explicitly correct for upper mantle anisotropy, null measurements do not necessarily imply that (in this case) *SKKS* phases have been unaffected by lowermost mantle anisotropy. However, it certainly means that *SKS* and *SKKS* phases are accumulating different splitting along their respective raypaths, perhaps sampling very different structures/fabric. As weakly discrepant measurements are omitted in Figure 7, most regions only display measurements from one backazimuthal swath.

5. Discussion and Modeling

5.1. Lowermost Mantle Structure and Anisotropy

Understanding the deformation geometry at the base of the mantle, as reflected in shear-wave splitting measurements, can help to decipher mantle flow patterns and eventually lead to insight into the origin and dynamics of structures such as LLSVPs. Previous studies have shown a substantial spatial correlation between regions with relatively strong lowermost mantle seismic anisotropy and the borders of LLSVPs, including both the African (Cottaar & Romanowicz, 2013; Lynner & Long, 2014; Wang & Wen, 2007) and the Pacific (Deng et al., 2017). Therefore, we also examine our observations in relation to the African LLSVP geometry. The locations of the LLSVPs, including their borders as well as heterogeneities within them, are generally well resolved by seismic tomography. However, there are some variations among models on smaller length scales (Garnero et al., 2016). Additional constraints come from waveform modeling and travel time analyses, which have mapped the eastern, southern, and western borders of the African LLSVP in detail (Wang & Wen, 2004; Wen, 2001).

We compare our measurements with lowermost mantle structure as expressed in the global *S* wave tomography model S40RTS (Ritsema et al., 2011) and in the model of Lekic et al. (2012), which uses cluster analysis to identify robust features across a suite of different tomography models. Figure 8 shows a map of all discrepant *SKS-SKKS* pairs identified in this study along with both views of the LLSVPs and provides a rich basis for detailed comparisons between anisotropic and isotropic lowermost mantle structure beneath Africa. We discuss these comparisons in detail in section 5.2, beginning in North Africa and working in a clockwise spiral. Beneath northern Africa (cluster A), most of our measurements sample the edge of the LLSVP as inferred by S40RTS (Figure 8a). Cluster B lies entirely outside the LLSVP with *SKS* pierce points close to the supposed root of the Afar plume, while cluster C consists of splitting pairs which cross the LLSVP border and pairs which lie outside. Cluster D, located beneath Central Africa, lies within the LLSVP.

In addition to comparing our splitting observations to tomographic models, we also undertake some simple forward modeling of plausible mantle deformation scenarios to explore mantle flow regimes that are consistent with our data, discussed further below. We use the MSAT toolbox (Walker and and Wookey, 2012) to test different plausible anisotropy scenarios that represent either CPO of candidate minerals or SPO of partial melt. MSAT predicts shear-wave splitting as a function of ray propagation by solving the Christoffel equation, under an assumption of ray theory. Given that we can only compare *SKS-SKKS* splitting intensity discrepancies and not actual fast directions and delay times, we limit our modeling to simple examples. In order to calculate approximate path lengths of each phase, we assume a straight line raypath approximation through the layer of anisotropy. We calculate the inclination angle of *SKS* and *SKKS* for a representative earthquake and station pair for each cluster (as identified in Figure 8). We calculate the pierce points at the CMB and the top of the D″ layer for each phase for the ak135 velocity model (Kennett et al., 1995) using the TauP toolkit (Crotwell et al., 1999). For each modeling scenario, we describe our underlying assumptions about deformation geometry in the sections below. We emphasize that the models we present are not intended to interrogate every possible mantle deformation geometry and anisotropy scenario; rather, we use them as specific and quantitative tests that particular mantle flow scenarios discussed in our interpretation are indeed consistent with the observations.

5.2. Anisotropy at the Northern Border of the LLSVP

Cluster A, beneath northern Africa, displays a typical geometry for most *SKS-SKKS* pairs in this region when compared to the tomographic model SR40TRS, in which one pierce point lies within the LLSVP interior and the other one in the fast/cold D″ region just outside it (see schematic diagram in Figure 9a). The cluster model (Figure 8b) shows a different LLSVP border compared to the SR40TRS model, suggesting that

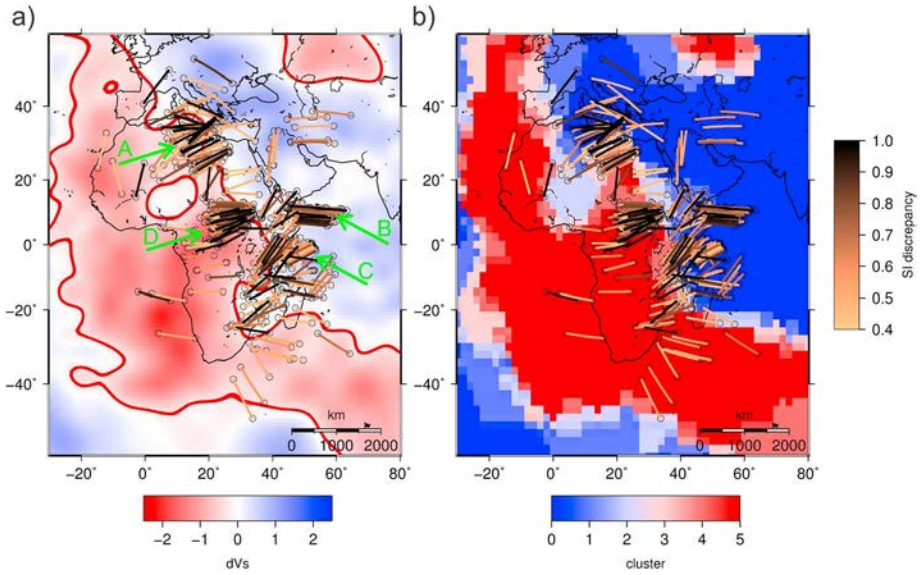

Figure 8. Highly discrepant *SKS-SKKS* pairs, as in Figure 6, plotted atop two different lower mantle models. (a) Background colors show shear velocities at a depth of 2,800 km in the global model SR40TRS (Ritsema et al., 2011). The LLSVP boundary, as defined by the 0.5% slow-velocity contour (Garnero et al., 2016), is denoted with a thick red line. Green arrows and labels denote specific regions discussed in section 4.3. (b) Background color shows the cluster model of Lekic et al. (2012), with the color bar showing the number of tomographic models (out of five) that agree that the shear velocity is anomalously slow at a given point.

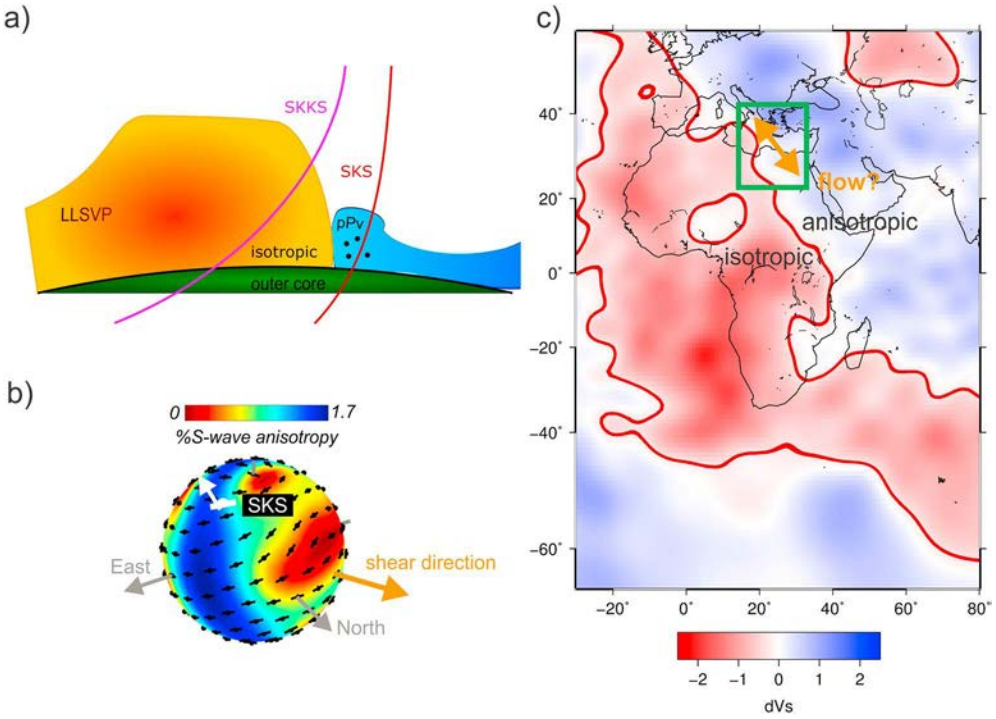

Figure 9. (a) Sketch of the proposed D″ structure at the LLSVP boundary with *SKS* and *SKKS* raypaths for the area denoted by the green box in (c). The dots in the cold D″ (visualized in blue) represent aligned postperovskite with a symmetry axis parallel to the core-mantle boundary and out of the paper plane. (b) A visual representation of a horizontally aligned deformed postperovskite tensor, which is sampled by an *SKS* phase propagating just outside the LLSVP boundary. Colors represent the strength of V_s anisotropy as a function of propagation direction, as indicated by the color bar. Black bars represent predicted fast splitting directions (in a ray reference frame) for different propagation directions. The orange arrow indicates the shear direction, which is horizontal (parallel to the core-mantle boundary). The raypath of the propagating *SKS* phase is shown by a white arrow, and the predicted splitting of the *SKS* phase is shown with a white bar. (c) Shear wave velocities (from the SR40RTS tomographic model; Ritsema et al., 2011) at 2,800-km depth. The LLSVP boundary, as defined by the 0.5% slow velocity contour (Garnero et al., 2016), is denoted with a thick red line. The orange arrow illustrates the shear direction as shown in (b), and the green box denotes the general area sampled by our observations.

different tomographic models have different features in this region. In this view, our pierce points seem to sample the LLSVP directly at the borders on both sides. We observe a smaller cluster with similar splitting characteristics (pierce points on either side of the boundary; *SKKS* are commonly null) in a backazimuth range between 0° and 45° at latitudes between 0° and −20° (Figure 7). Here tomographic models agree on the location of the LLSVP boundary.

At first glance, our observations beneath northern Africa are consistent with the major conclusion of Lynner and Long (2014), who found that strongest lowermost mantle anisotropy tends to be located near the LLSVP border. Our findings highlight a possible change in anisotropic characteristics between the pierce points and could be interpreted as being consistent with those of Cottaar and Romanowicz (2013), who found that anisotropy is strong outside the LLSVP but absent inside the LLSVP (see also Lynner & Long, 2014). Anisotropy in the (presumably colder) portion of D″ outside the LLSVP would be expected in regions experiencing strong deformation, consistent with the scenario in which the anisotropic fabric reflects CPO due to dislocation creep in a cold, high-stress downwelling (e.g., McNamara et al., 2001, 2002; Cottaar & Romanowicz, 2013; Cottaar et al., 2014). Close to the LLSVP borders, strong deformation may also be expected if LLSVPs are indeed thermochemical piles that are created by convective flow. Increased strain could plausibly accumulate at the LLSVP borders and lead to either CPO or SPO of elastically distinct material (e.g., Garnero et al., 2016).

We test these hypotheses by forward modeling expected shear-wave splitting due to an anisotropic layer outside the LLSVP. While ferropericlase and bridgmanite are possible candidates for anisotropy in the D″ layer, we only consider an elastic tensor representing textured postperovskite, both for simplicity and because postperovskite is thought to be a more likely mechanism (e.g., Creasy et al., 2017; Ford et al., 2015; Nowacki et al., 2011; Walker et al., 2011). In order to represent the anisotropy of deformed postperovskite, we use an elastic tensor derived from viscoplastic self-consistent modeling as shown in Figure 9b. This tensor was produced by deforming postperovskite in simple shear with a dominant slip system of [100](010), as proposed by Miyagi et al. (2010), using the single-crystal elasticity of postperovskite at 125 GPa from Wentzcovitch et al. (2006). Many observational studies have indicated that this slip system most likely dominates for postperovskite, based on the fit between predictions and observations (e.g., Ford and Long, 2015; Walker et al., 2011). This elastic tensor does not predict any splitting of the *SKS* phase for vertical flow in a simple shear geometry. However, horizontal simple shear does predict significant *SKS* splitting (and therefore discrepant *SKS*-*SKKS* splits, if the *SKKS* phases sample an isotropic LLSVP interior), with the strongest splitting predicted for a range of shear directions at azimuths of 160–360°. Based on this simple modeling, we suggest that a plausible geodynamic flow scenario for the cluster A region (Figure 9) is horizontal mantle flow that is parallel to the LLSVP edge, or perhaps deflected by it (and thus oblique to the edge). Our modeling suggests that vertically deflected flow just outside the LLSVP is implausible in this region, unless a different slip system dominates in postperovskite. Alternatively, our explanations could be explained if there is anisotropy within the LLSVP itself, leading to splitting of the *SKKS* phases, but the flow just outside the LLSVP is in a geometry that does not produce *SKS* splitting. Further work is necessary to distinguish between these different hypothesis, particularly work that explicitly removes the effect of upper mantle anisotropy on the *SK*(*K*)*S* phases we study here.

5.3. Mantle Flow Outside of the LLSVP Beneath Afar

To the east of the Afar region, beneath the western Indian Ocean, we document a cluster (cluster B in Figure 8) of strongly discrepant *SKS*-*SKKS* pairs that sample entirely within the cold/fast part of the D″ region. Most of these measurements have significantly split *SKS* and *SKKS* phases, with some pairs that display a split *SKS* and a null *SKKS* clustered at the very eastern edge of this group. The *SKS* pierce points for this group of pairs are proximal to an area of the lowermost mantle whose anisotropy was previously considered by Ford et al. (2015). That study incorporated splitting measurements for different seismic phases over a range of backazimuths and implemented some simplified forward modeling of these measurements. They concluded that anisotropy outside the LLSVP edge is best explained by postperovskite CPO, with the [100] crystallographic axes preferentially oriented nearly vertically or highly obliquely to the horizontal plane. This may indicate vertical flow deflected by the LLSVP boundary, sheet-like upwellings, and/or a lateral change in flow geometry (Ford et al., 2015).

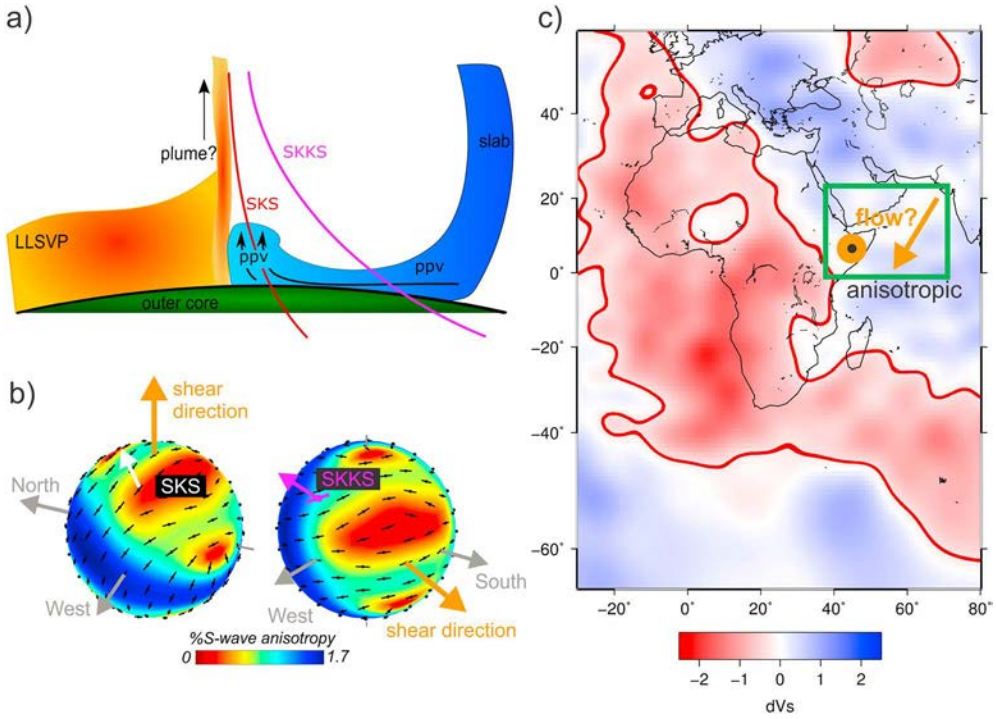

Figure 10. (a) Sketch of the proposed D″ structure at the LLSVP boundary with *SKS* and *SKKS* raypaths for the area denoted by the green box in (c). (b, left) A visual representation of a vertically aligned tensor representing textured postperovskite, which is sampled by an *SKS* phase, as shown in (a). The raypath of the propagating *SKS* phase is shown by a white arrow. The orange arrow denotes a vertical shear direction (perpendicular to the core-mantle boundary). Colors represent the strength of V_s anisotropy as a function of direction, as indicated by the color bar. Black bars represent predicted fast splitting directions (in a ray reference frame) for different propagation directions. (right) A visual representation of a horizontally aligned tensor representing textured postperovskite, which is sampled by *SKKS*. The raypath of the propagation *SKKS* phase is shown in purple. The orange arrow denotes a horizontal shear direction (parallel to the core-mantle boundary). c) Shear-wave velocities (from the SR40RTS tomographic model; Ritsema et al., 2011) at 2,800-km depth. The LLSVP boundary, as defined by the 0.5% slow-velocity contour (Garnero et al., 2016), is denoted with a thick red line. The orange arrow and circle illustrate the change in shear direction, as represented in (b), and the green box denotes the general area sampled by our observations.

Our finding of strongly discrepant *SKS-SKKS* splitting in this region is generally consistent with the anisotropy scenarios proposed by Ford et al. (2015). Furthermore, given the proximity of this group to the Afar plume, which is often considered to be rooted in the lowermost mantle (e.g., Courtillot et al., 2003; Montelli et al., 2004), we propose that our discrepant *SKS-SKKS* observations from the Afar/Indian Ocean cluster may reflect a lateral transition from horizontal flow to vertical flow at the base of the plume. Because our measurement method does not directly reflect the actual geometry of anisotropy at the base of the mantle, our measurements are not definitive; however, it is plausible that our measurements sample such a transition in flow.

We test this idea by carrying out a simple forward model of this flow scenario, using the same elastic tensor for textured postperovskite tensor as in section 5.2, assuming deformation by horizontal shear sampled by the *SKKS* phase and vertical shear for the *SKS* phase. Figure 10a shows a sketch of their respective raypaths and proposed flow regime, while Figure 10b shows visual representations of the respective postperovskite tensors. We found through this modeling exercise that vertically sheared postperovskite aggregate, or one deformed in a tilted geometry, *SKS* should undergo only weak splitting. However, a horizontally sheared postperovskite aggregate should produce strong splitting for the *SKKS* phase for most propagation azimuths, except for wave propagation parallel to the shear direction. While a range of horizontal shear directions should produce splitting of the *SKKS* phase, we suggest that a likely scenario is mantle flow toward the root of the putative Afar plume, roughly perpendicular to the LLSVP edge, as shown in Figure 10c. While we do not claim that this is the only model that can explain the observations, the forward models shown in

Figure 10 reveal that this flow scenario is generally consistent with the splitting observations and is also consistent with the inferences on flow beneath the Afar plume suggested by Ford et al. (2015).

Returning to the argument that LLSVPs might be passive features that are swept around by remnant slabs, Steinberger and Torsvik (2012) used geodynamical modeling to show that subduction-driven horizontal flow at the base of the mantle may drive the formation of sheet-like upwellings at the border of the LLSVP, which may further evolve into single plumes in the upper mantle. This flow transition, shown in cartoon view in Figure 10a, would predict a lateral change in lowermost mantle anisotropy, which would be reflected by discrepant *SKS-SKKS* splitting. This view is consistent with the findings of Ford et al. (2015) and supports the hypothesis that LLSVPs represent long-lived thermochemical boundaries that are swept together by slabs that then pile up at the border of the LLSVPs. A similar argument may hold for a smaller cluster of (slightly less strongly) discrepant *SKS-SKKS* pairs in our data set, which samples directly to the south of the large cluster (see cluster C in Figure 8) and lies well outside the LLSVP boundary. Interestingly, this set of measurements is also associated with a strong dependence of splitting intensity discrepancies with backazimuth.

Beneath the southern part of the Mozambique Channel, the SR40TRS and cluster models disagree somewhat on the geometry of the LLSVP boundary, with S40RTS displaying a dent or divot in the LLSVP. Our measurements are sparser here and may sample either inside (suggested by the cluster model) or mostly outside (suggested by S40RTS) the LLSVP. Further to the south, both models show a consistent shape of the LLSVP border. Our measurements in this region partially corroborate the findings of Lynner and Long (2014), who found only nondiscrepant pairs in the southern portion of the African LLSVP (as inferred from the Lekic et al., 2012, cluster model). Our data set shows only a few scattered discrepant measurements and many nondiscrepant ones in this region. On the other hand, Wang and Wen (2007) found complex anisotropy beneath the southern part of the Mozambique Channel, which they associated with the LLSVP border. Differences between our data set and theirs may arise from the different definitions of discrepant measurements used (splitting intensity in our study, splitting parameters in the earlier work) or the fact that Wang and Wen (2007) do not use pairs of phases from the same seismograms.

5.4. Anisotropy Within the LLSVP Interior and Its Possible Relationship to ULVZs

We now consider the interpretation of the group of strongly discrepant measurements that we identified beneath Central Africa, to the west of the Afar Peninsula (cluster D in Figure 8). Beneath this region, the LLSVP borders are similarly defined by S40TRS and the cluster model (Figure 8). The pierce points for this strongly discrepant cluster beneath Central Africa lie mostly within the LLSVP itself, with the eastern pierce points located close to its border. For this group of measurements, the *SKKS* measurements (which sample to the west of the *SKS* pierce points) are either null or split, while the majority of *SKS* phases are split. This set of measurements is notable, as this region has not been studied in detail by previous work on *SKS-SKKS* discrepancies beneath Africa; furthermore, it seems to represent a fairly unusual observation of strong lowermost mantle anisotropy in the interior of an LLSVP. We consider two possible explanations for this unusual observation.

First, if the LLSVP interior is indeed generally isotropic as suggested by previous studies, then our observations could perhaps be explained if the boundary of the LLSVP is incorrectly captured by the tomographic models and in fact lies further to the west than indicated in Figure 8. If this were the case, then the *SKS* phases for this group of measurements could be sampling strong anisotropy just outside the LLSVP border, while the associated *SKKS* could be sampling isotropic lowermost mantle in the LLSVP interior. We have previously demonstrated that a *SKS* phase traveling through a vertically sheared postperovskite right outside the LLSVP boundary does not undergo significant splitting (assuming the most likely dominant slip system). Given this constraint, we infer a few plausible scenarios: One is that the *SKS* phases for this cluster, sampling just outside the LLSVP, do not experience splitting, while the *SKKS* phase is significantly split to allow for the highly discrepant measurements we observe. A second possibility is that the flow just outside the LLSVP boundary sampled by cluster D is horizontal, as we infer for the northern boundary of the LLSVP (section 5.2), while the LLSVP interior is isotropic. However, pierce points outside the LLSVP for this cluster lie close to the supposed root of the Afar plume, which might favor the idea of vertical flow at this location.

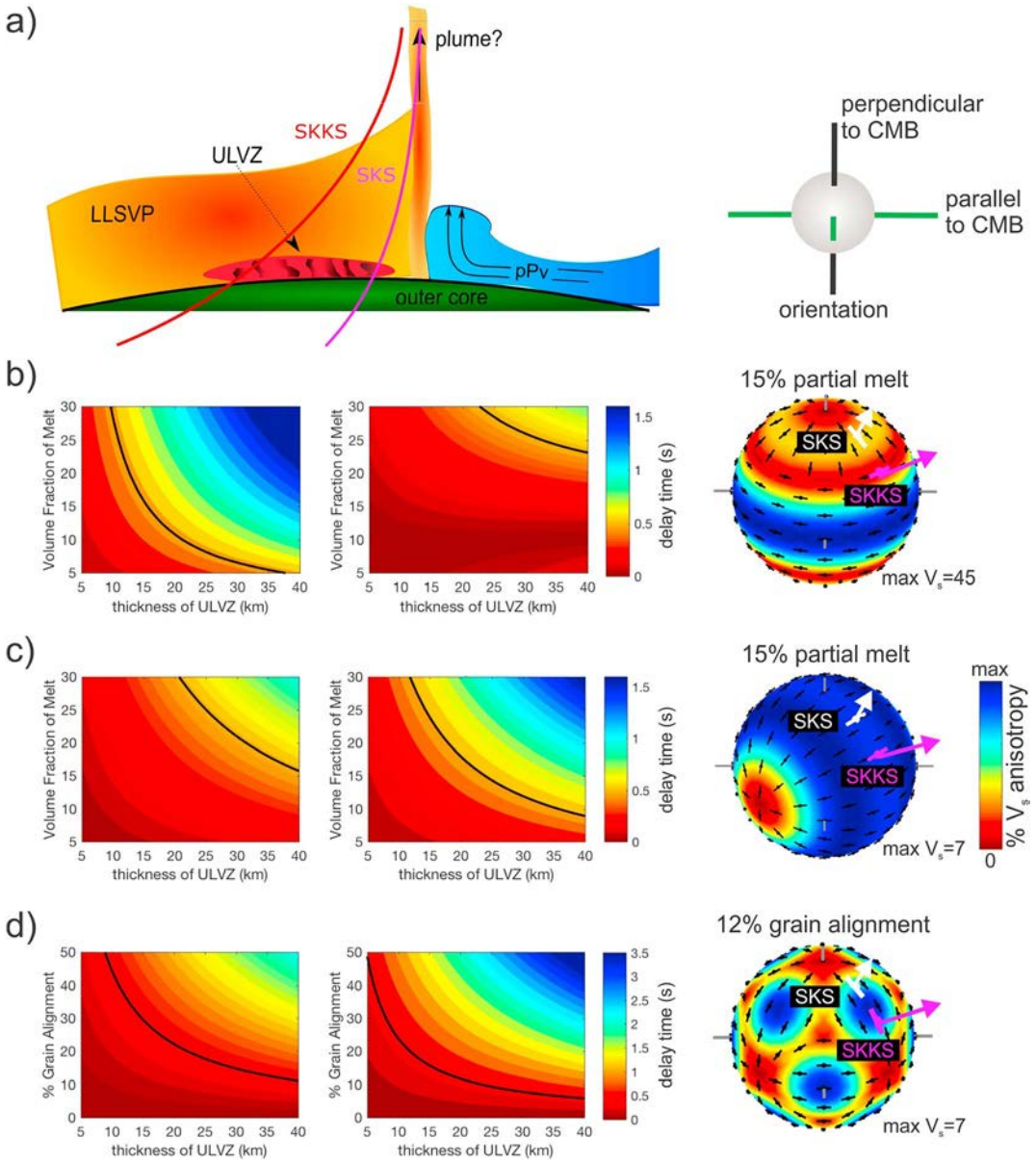

Figure 11. Seismic anisotropy induced by a ULVZ that is dominated by aligned partial melt. (a) Sketch of raypaths through the proposed ULVZ structure. (b) Predictions of shear-wave splitting delay time (colors, as represented by the color bar at the right) for disk-shaped SPO for (left) *SKS* phases and (middle) *SKKS* phases as a function of partial melt fraction (*y* axes) and ULVZ thickness (*x* axes). The solid black line shows the contour of 0.5 s delay time. (right) A visual representation of the horizontally aligned elastic tensor, along with splitting predictions, for 15% partial melt fraction. Colors represent strength of V_s anisotropy as a function of ray propagation direction. Raypaths of propagating *SKS* and *SKKS* phases are shown in white and magenta, respectively. Black bars represent predicted fast splitting directions in ray-reference frame for a range of propagation directions. (c) Predictions of shear-wave splitting delay time for cigar-shaped SPO. Plotting conventions are as in (b). (d) Predicted splitting delay times for an iron-rich ferropericlase (Finkelstein et al., 2018). (left and middle) Predicted delay times are shown as a function of grain alignment (in % of grains aligned, *y* axis) and ULVZ thickness (*x* axis). (right) The splitting predictions for an elastic tensor with 12% of grains aligned.

Another intriguing possibility is that the group of strongly discrepant measurements beneath Central Africa do, in fact, reflect strong lowermost mantle anisotropy within the LLSVP itself, sampled either by only the *SKKS* phase or by both phases (see sketch in Figure 11a). Possible mechanisms for D″ anisotropy within the LLSVP are uncertain; while lowermost mantle anisotropy is often attributed to CPO of postperovskite,

this phase may not be stable in the slower and presumably hotter parts of D″ (e.g., Houser, 2007). Alternative models include CPO of other phases such as bridgmanite or ferropericlase or SPO of compositional heterogeneities or melt inclusions. In a recent study, Koelemeijer et al. (2018) found that their tomographic model SP12RTS is best reproduced by global mantle flow models if it is assumed that postperovskite exits everywhere in the D″, even in the (slower and hotter) LLSVPs. This contradicts earlier findings but opens up the possibility of CPO from postperovskite inside the LLSVPs, although an aligned texture has to be present to result in an anisotropy measurable over seismic wavelengths (e.g., Nowacki et al., 2011). Because CPO is accumulated through strain due to deformation accommodated by dislocation creep (e.g., McNamara et al., 2001, 2002), this potential explanation for our observations beneath Central Africa would imply substantial deformation in the dislocation creep regime within the LLSVP interior. Given the proposed longevity of LLSVPs, internal convection might have developed through basal heating and the incorporation of new material from cold slabs, leading to significant mantle flow (Li et al., 2014; Mulyukova et al., 2015). Considering the geometry of the raypaths in this cluster, significant discrepancies could be caused by a change in flow geometry analogous to the scenario explored in section 5.3.

Another plausible explanation for our observations suggesting strong anisotropy within the central portion of the African LLSVP is suggested by the geographical coincidence between our splitting discrepancies and an ULVZ at the base of the mantle, as documented by Ni and Helmberger (2001) and included in the global compilation of Yu and Garnero (2018). Ni and Helmberger (2001) mapped this region to be a ridge-like, north-south oriented structure with a length of 800 km and a width between 250 and 400 km and an *S* wave velocity drop up to 30%. The thicknesses of ULVZs vary globally but are generally found to be between 5 and 40 km (Garnero et al., 2016). During our splitting analysis, we noticed very large delays in *SK*(*K*)*S* arrival times compared to the theoretical phase arrival (as calculated for the iasp91 global model), as well as a certain amount of *SK*(*K*)*S* pulse broadening, supporting the argument that some of our waveforms may sample ULVZ material. It is unclear precisely how ULVZs interact with the LLSVPs, but it is commonly thought that ULVZs are partially molten and chemically distinct from the surrounding mantle (Yu & Garnero, 2018, and references therein), although other models for ULVZs do exist (e.g., Bower et al., 2011; Wicks et al., 2010). There are several plausible scenarios for strong anisotropy associated with a ULVZ region. One possibility is strong anisotropy due to SPO of aligned partial melt within the ULVZ (e.g., Garnero et al., 2016). A second possibility invokes strong anisotropy in particularly iron-rich magnesiowüstite (Finkelstein et al., 2018), which may explain both the dramatic velocity reduction associated with a ULVZ and the strong anisotropy suggested by our *SKS-SKKS* discrepancy measurements.

We test these ideas by forward modeling different elastic tensors that represent the different proposed causes of ULVZs: (i) SPO of partial melt, assuming alignment in cigar- and disk-shaped configurations, and (ii) iron-rich magnesiowüstite (see Figure 11). First, we examine predicted splitting for partial melt scenarios. We examine a range of tensors, for which we vary the melt content (between 5% and 30% by volume; Yu & Garnero, 2018) and ULVZ layer thickness (from 5 to 40 km; Yu & Garnero, 2018). We assume that the melt is neutrally buoyant and thus dynamically stable; however, the density of melt has little to no effect on the strength or pattern of anisotropy. We use the approach of effective medium theory, as developed by Tandon and Wenig (1984) and implemented in MSAT (Walker & Wookey, 2012), to calculate elastic tensors. For an oblate SPO (disk shape), *SKS* can undergo relatively strong splitting (greater than 0.5 s delay times) under a variety of scenarios, ranging from a thin (10–15 km) ULVZ with greater than 15% melt or a thick (30–40km) ULVZ with only 5% melt. For these scenarios, however, *SKKS* is not predicted to undergo strong splitting (Figure 11b). For tubule SPO, our models predict that both *SKS* and *SKKS* could plausibly be split; however, the partial melt fraction must be at least 8% (for *SKKS*) to 15% (for *SKS*), as shown in Figure 11c. Overall, for reasonable partial melt fractions and ULVZ layer thicknesses, we find that both *SKS* and *SKKS* phases could plausibly undergo splitting due to a ULVZ. This possibility can be explored further by future work on the attenuation structure of the lowermost mantle in this region, as the presence of partial melt might lead to enhanced attenuation of shear waves.

Next, we examine CPO from iron-rich ferropericlase as a possible mechanism for anisotropy in ULVZs. Finkelstein et al. (2018) measured the elastic parameters of a single crystal of (Mg,Fe)O magnesiowüstite with 76 mol% FeO at 41 GPa. This work demonstrated that the strength of anisotropy for iron-bearing ferropericlase is higher than that for iron-poor ferropericlase. Here we use the measured elasticity at their

maximum experimental pressure of 41 GPa as most nearly representative of anisotropy at D″ pressures. In order to produce anisotropy, aggregates containing ferropericlase must undergo deformation under deformation creep; however, the dominant slip systems are poorly known. Rather than explicitly modeling texture development in this mineral, we use the single-crystal elastic constants and vary the strength of anisotropy by varying the grain alignment in a hypothetical aggregate. We conduct Voigt-Reuss-Hill averaging of elasticity by mixing the isotropic component of the elastic tensor with the anisotropic component, in varying proportions. We explore grain alignments from 0% to 50% (see Figure 11d). We find that only very small grain alignments (<10% and 15%) are needed to induce splitting of *SKKS* and *SKS* phases, respectively. Since single crystals of iron-bearing ferropericlase are strongly anisotropic, only weak crystal alignments are needed to produce significant splitting even for relatively thin ULVZ layers. We note, however, that relatively long-wavelength *SK*(*K*)*S* phases (dominant periods of ~10–12 s) may not be sensitive to very thin ULVZ structures of ~5-km thickness or less. In general, however, the modeling shown in Figure 11 demonstrates that textured iron-rich ferropericlase in ULVZs can plausibly explain our splitting intensity discrepancy observations in cluster D.

Interestingly, ULVZs have a tendency to be located close to the edges of the LLSVPs and to deep rooted mantle plumes (Yu & Garnero, 2018), although the latter relationship may not be statistically robust. Deep mantle plumes are, in turn, often observed at the border of the LLSVPs (Burke et al., 2008). Geodynamical modeling suggests that if LLSVPs are indeed thermochemical piles, ULVZs will be swept toward the margins of the LLSVPs over time (e.g., Hernlund & McNamara, 2015). If that is the case, this may also introduce strong deformation at the base of the mantle, and the resulting strain could produce CPO; this scenario could explain aspects of our data set. Our observations of lowermost mantle anisotropy associated both with the ULVZ beneath Central Africa and with the possible root of the Afar plume, just to the east, may also be consistent with recent findings that explore the spatial coincidence of ULVZ material and deep mantle plumes. For example, French and Romanowicz (2015) have shown that the hot spots of Hawaii, Iceland, and Samoa seem to be rooted in areas of greatly reduced shear velocity that coincide with large ULVZs. A perhaps analogous region of our own study area (the ULVZ beneath Central Africa and the nearly adjacent Afar plume) may express similar processes in the anisotropic structure. Our work may therefore help to inform our evolving view of how ULVZs and plume source regions are dynamically linked; while our observations cannot definitively characterize the geometry of lowermost mantle anisotropy, they are generally consistent with the mantle flow scenario shown in Figure 12.

6. Conclusions

We analyzed data from all permanent and temporary seismic station deployments in Africa and surrounding regions since 1990, with the goal of identifying *SKS*-*SKKS* pairs for which shear-wave splitting could be confidently resolved. We performed splitting analyses using both the transverse energy minimization and splitting intensity methods to identifying possibly discrepant *SKS*-*SKKS* pairs that indicate a contribution to splitting from seismic anisotropy at the base of the mantle. Our set of 896 robust *SKS*-*SKKS* pairs represents one of the largest and most comprehensive data sets yet assembled to probe lowermost mantle anisotropy beneath Africa. We found that roughly one third of our measurements involve significant discrepancies in splitting intensity values between the *SKS* and *SKKS* phases. In map view, our strongly discrepant pairs are generally localized in specific areas: at the northern and southeastern borders of the LLSVP, inside the LLSVP beneath Central Africa, and outside of the LLSVP just to the east of the Afar peninsula (and near the putative source region of the Afar plume).

To explain these observations, we invoke different mechanisms for flow and the resulting seismic anisotropy in each setting (see Figure 12 for a sketch). Discrepant pairs that sample across the border of the LLSVP are consistent with a scenario in which one set of phases samples the dominantly isotropic interior of the LLSVP, while the other set samples strong anisotropy just outside the LLSVP border. This idea is consistent with the suggestions of previous studies, although we find that the deformation just outside the northern border of the African LLSVP is likely horizontal and not vertical. Observations of strong discrepancies within the LLSVP beneath Central Africa are notable because of the geographic overlap with a previously mapped ULVZ. Plausible mechanisms for anisotropy in this region include SPO of partial melt or compositional heterogeneities inside the ULVZ or strong anisotropy of iron-rich magnesiowüstite. If postperovskite is present

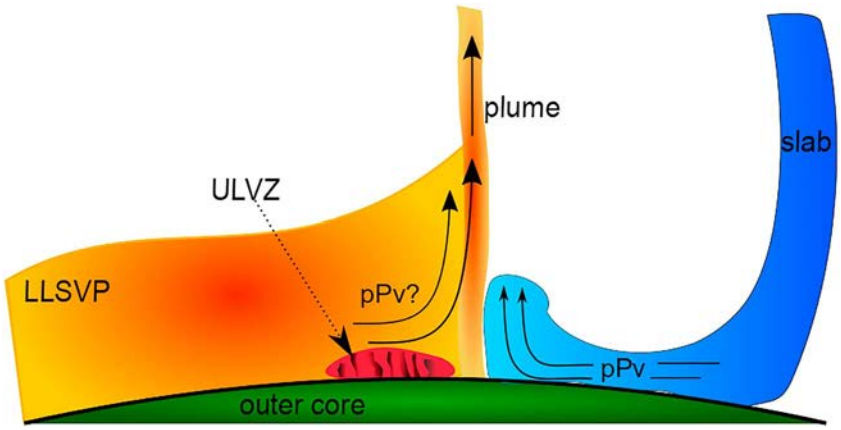

Figure 12. Sketch of proposed flow geometries and anisotropic structures (not to scale) that can plausibly explain the SKS-*SKKS* splitting discrepancies documented in this study.

within the LLSVP interior, as suggested by some previous work, then CPO of postperovskite may also represent a viable explanation for anisotropy beneath Central Africa. Each of these scenarios is consistent with our observations, as demonstrated by our forward modeling, but distinguishing among them will require additional observations. Finally, our observations of discrepant pairs just outside the LLSVP boundary, beneath the Afar region, likely elucidate a change in the flow geometry from horizontal to vertical, consistent with upwelling just outside the LLSVP edge.

Taken together, our observations are consistent with the view, advocated by previous geodynamical modeling studies, that LLSVPs are passive thermochemical piles whose locations and characteristics are controlled by subducting slabs impinging on the CMB. In this view, subduction-driven horizontal flow at the base of the mantle induces a vertical flow component at the LLSVP boundary, as flow is deflected at the LLSVP edge. Within the LLSVP, ULVZs may slowly be swept toward the LLSVP boundary. This general view may explain our observation of strong *SKS-SKKS* splitting discrepancies in several distinct regions in and around the African LLSVP; however, we caution that by themselves, our *SKS-SKKS* discrepancy measurements are not definitive, because they cannot constrain the actual geometry of D″ anisotropy. Further work that incorporates additional data from, for example, the splitting of *S-ScS* phases, is needed to sample lowermost mantle anisotropy beneath Africa over a range of propagation directions and to test the flow scenarios proposed in this study.

Data

Raw data used in this study were downloaded through the International Federation of Digital Seismograph Networks Web Services (https://www.fdsn.org/webservices/). The data for the following networks are provided by the Incorporated Research Institutions for Seismology (IRIS) Data Management Center (http://www.iris.edu): 1C (https://doi.org/10.7914/SN/1C_2011), 2H (https://doi.org/10.7914/SN/2H_2009), 3D (https://doi.org/10.7914/SN/3D_2010), AF (https://doi.org/10.7914/SN/AF), G (https://doi.org/10.18715/GEOSCOPE.G), GH (Ghana Digital Seismic Network), GT (https://doi.org/10.7914/SN/GT), II (https://doi.org/10.7914/SN/II), IU (https://doi.org/10.7914/SN/IU), MN (https://doi.org/10.13127/SD/fBBBtDtd6q), TT (Seismic Network of Tunisia), XA (https://doi.org/10.7914/SN/XA_1997), XB (https://doi.org/10.7914/SN/XB_2005; https://doi.org/10.7914/SN/XB_2009), XD (https://doi.org/10.7914/SN/XD_1994), XI (https://doi.org/10.7914/SN/XI_1995; https://doi.org/10.7914/SN/XI_2000), XJ (https://doi.org/10.7914/SN/XJ_2013), XK (https://doi.org/10.7914/SN/XK_2012), XV (https://doi.org/10.7914/SN/XV_2011), XZ (https://doi.org/10.7914/SN/XZ_2003), YH, YJ, YQ (https://doi.org/10.7914/SN/YQ_2013), YR (https://doi.org/10.15778/RESIF.YR1999; Dhofar Seismic Experiment II), YY (https://doi.org/10.7914/SN/YY_2013), YZ (Boina Broadband Network), ZE (https://doi.org/10.7914/SN/ZE_2007), ZF (Afar Consortium Network), ZK (https://doi.org/10.7914/SN/ZK_2009), ZP (https://doi.org/10.7914/SN/ZP_2007), and ZV (https://doi.org/10.7914/SN/ZV_2014). IRIS Data Services are funded through the

Seismological Facilities for the Advancement of Geoscience and EarthScope (SAGE) Proposal of the National Science Foundation under Cooperative Agreement EAR-1261681. The data for the following networks are hosted by GEOFON (https://geofon.gfz-potsdam.de/): 1B (Uganda project), GE (https://doi.org/10.14470/TR560404), Z5 (RiftLink), and ZE (https://doi.org/10.14470/MR7567431421). Measurements of splitting intensity and splitting parameters for *SKS-SKKS* pairs presented in this study can be found in supporting information Table S1 and are archived in the Zenodo scientific data repository (zenodo.org, https://doi.org/10.5281/zenodo.2671723).

Acknowledgments
M. C. Reiss was supported by a postdoctoral fellowship of the German Academic Exchange Service (DAAD). M. D. Long acknowledges support from the U.S. National Science Foundation (NSF) via grant EAR-1547499, and N. C. acknowledges support from NSF Graduate Research Fellowship grant DGE-1122492. We thank Georg Rümpker for access to the restricted data sets of the Uganda project, RiftLink and SELASOMA (https://doi.org/10.14470/MR7567431421). We thank Cindy Ebinger and Derek Keir for access to the restricted data set of the Southern Lake Tanganyika experiment (https://doi.org/10.7914/SN/ZV_2014). We are grateful to Lowell Miyagi for sharing the elastic tensors for postperovskite aggregates used in the modeling. This work benefitted from helpful discussions with Andrea Tesoniero and Elvira Mulyukova and from thoughtful comments from two anonymous reviewers.

References

Austermann, J., Kaye, B. T., Mitrovica, J. X., & Huybers, P. (2014). A statistical analysis of the correlation between large igneous provinces and lower mantle seismic structure. *Geophysical Journal International*, *197*(1), 1–9. https://doi.org/10.1093/gji/ggt500

Bagley, B., & Nyblade, A. A. (2013). Seismic anisotropy in eastern Africa, mantle flow, and the African superplume. *Geophysical Research Letters*, *40*, 1500–1505. https://doi.org/10.1002/grl.50315

Barruol, G., & Fontaine, F. R. (2013). Mantle flow beneath La Réunion hotspot track from SKS splitting. *Earth and Planetary Science Letters*, *362*, 108–121. https://doi.org/10.1016/j.epsl.2012.11.017

Barruol, G., & Hoffmann, R. (1999). Upper mantle anisotropy beneath Geoscope stations. *Journal of Geophysical Research*, *104*(B5), 10,757–10,773. https://doi.org/10.1029/1999JB900033

Becker, T. W., Conrad, C. P., Schaeffer, A. J., & Lebedev, S. (2014). Origin of azimuthal seismic anisotropy in oceanic plates and mantle. *Earth and Planetary Science Letters*, *401*, 236–250. https://doi.org/10.1016/j.epsl.2014.06.014

Becker, T. W., Lebedev, S., & Long, M. D. (2012). On the relationship between azimuthal anisotropy from shear wave splitting and surface wave tomography. *Journal of Geophysical Research*, *117*(B1), B01306. https://doi.org/10.1029/2011JB008705

Bower, D. J., Wicks, J. K., Gurnis, M., & Jackson, J. M. (2011). A geodynamic and mineral physics model of a solid-state ultralow-velocity zone. *Earth and Planetary Science Letters*, *254*(1-2), 233–238. https://doi.org/10.1016/j.epsl.2006.11.025

Burke, K., Steinberger, B., Torsvik, T. H., & Smethurst, M. A. (2008). Plume generation zones at the margins of large low shear velocity provinces on the core–mantle boundary. *Earth and Planetary Science Letters*, *265*(1-2), 49–60. https://doi.org/10.1016/j.epsl.2007.09.042

Chevrot, S. (2000). Multichannel analysis of shear wave splitting. *Journal of Geophysical Research*, *105*(B9), 21,579–21,590. https://doi.org/10.1029/2000JB900199

Cottaar, S., & Romanowicz, B. (2013). Observations of changing anisotropy across the southern margin of the African LLSVP. *Geophysical Journal International*, *195*(2), 1184–1195. https://doi.org/10.1093/gji/ggt285

Courtillot, V., Davaille, A., Besse, J., & Stock, J. (2003). Three distinct types of hotspots in the Earth's mantle. *Earth and Planetary Science Letters*, *205*(3–4), 295–308. https://doi.org/10.1016/S0012-821X(02)01048-8

Creasy, N., Long, M. D., & Ford, H. A. (2017). Deformation in the lowermost mantle beneath Australia from observations and models of seismic anisotropy. *Journal of Geophysical Research: Solid Earth*, *122*, 5243–5267. https://doi.org/10.1002/2016JB013901

Crotwell, H. P., Owens, T. J., & Ritsema, J. (1999). The TauP Toolkit: Flexible seismic travel-time and ray-path utilities. *Seismological Research Letters*, *70*(2), 154–160. https://doi.org/10.1785/gssrl.70.2.154

Davaille, A. (1999). Simultaneous generation of hotspots and superswells by convection in a heterogeneous planetary mantle. *Nature*, *402*(6763), 756–760. https://doi.org/10.1038/45461

Deng, J., Long, M. D., Creasy, N., Wagner, L. S., Beck, S. L., & Tavera, H. (2017). Lowermost mantle anisotropy near the eastern edge of the Pacific large low shear velocity province: Constraints from SKS-SKKS splitting intensity discrepancies. *Geophysical Journal International*, *210*(2), 774–786. https://doi.org/10.1093/gji/ggx190

Finkelstein, G. J., Jackson, J. M., Said, A., Alatas, A., Leu, B. M., Sturhahn, W., & Toellner, T. S. (2018). Strongly anisotropic magnesiowüstite in Earth's lower mantle. *Journal of Geophysical Research: Solid Earth*, *123*(6), 4740–4750. https://doi.org/10.1029/2017JB015349

Ford, H. A., Long, M. D., He, X., & Lynner, C. (2015). Lowermost mantle flow at the eastern edge of the African large low shear velocity province. *Earth and Planetary Science Letters*, *420*, 12–22. https://doi.org/10.1016/j.epsl.2015.03.029

French, S. W., & Romanowicz, B. (2015). Broad plumes rooted at the base of the Earth's mantle beneath major hotspots. *Nature*, *525*(7567), 95–99. https://doi.org/10.1038/nature14876

Gao, S. S., Liu, K. H., & Abdelsalam, M. G. (2010). Seismic anisotropy beneath the Afar depression and adjacent areas: Implications for mantle flow. *Journal of Geophysical Research*, *115*. https://doi.org/10.1029/2009JB007141

Garnero, E. J., McNamara, A. K., & Shim, S.-H. (2016). Continent-sized anomalous zones with low seismic velocity at the base of Earth's mantle. *Nature Geoscience*, *9*(7), 481–489. https://doi.org/10.1038/NGEO2733

Hammond, J. O. S., Kendall, J.-M., Rümpker, G., Wookey, J., Teanby, N., Joseph, P., et al. (2005). Upper mantle anisotropy beneath the Seychelles microcontinent. *Journal Geophysical Research Solid Earth: Solid Earth*, *110*(B11), B11401. https://doi.org/10.1029/2005JB003757

Hanna, J., & Long, M. (2012). SKS splitting beneath Alaska: Regional variability and implications for subduction processes at a slab edge. *Tectonophysics*, *530-531*, 272–285. https://doi.org/10.1016/j.tecto.2012.01.003

Hernlund, J. W., & McNamara, A. K. (2015). The core-mantle boundary region. *Treatise on Geophysics*, *2*(7), 461–519. https://doi.org/10.1016/B978-0-444-53802-4.00136-6

Hirose, K., Wentzcovitch, R., Yuen, D. A., & Lay, T. (2015). Mineralogy of the deep mantle—The post-perovskite phase and its geophysical significance. *Treatise on Geophysics*, 85–115. https://doi.org/10.1016/B978-0-444-53802-4.00054-3

Homuth, B., Löbl, U., Batte, A. G., Link, K., Kasereka, C. M., & Rümpker, G. (2014). Seismic anisotropy of the lithosphere/asthenosphere system beneath the Rwenzori region of the Albertine Rift. *International Journal of Earth Sciences*, *105*(6), 1681–1692. https://doi.org/10.1007/s00531-014-1047-0

Houser, C. (2007). Constraints on the presence or absence of post-perovskite in the lowermost mantle from long-period seismology. In K. Hirose, J. Brodholt, T. Lay, & D. Yuen (Eds.), *Post-perovskite: The last mantle phase transition, Geophysical Monograph Series*, (Vol. 174, pp. 191–216). Washington, DC: American Geophysical Union.

Karato, S.-I., Jung, H., Katayama, I., & Skemer, P. (2008). Geodynamic significance of seismic anisotropy of the upper mantle: New insights from laboratory studies. *Annual Reviews Earth and Planetary Science*, *36*(1), 59–95. https://doi.org/10.1146/annurev.earth.36.031207.124120

Kennett, B. L. N., Engdahl, E. R., & Buland, R. (1995). Constraints on seismic velocities in the Earth from traveltimes. *Geophysical Jounral International*, *122*(1), 108–124. https://doi.org/10.1111/j.1365-246X.1995.tb03540.x

Koelemeijer, P., Schuberth, B. S. A., Davies, D. R., Deuss, A., & Ritsema, J. (2018). Constraints on the presence of post-perovskite in Earth's lowermost mantle from tomographic-geodynamic model comparisons. *Earth and Planetary Science Letters*, *494*, 226–238. https://doi.org/10.1016/j.epsl.2018.04.056

Lekic, V., Cottaar, S., Dziewonski, A. M., & Romanowicz, B. (2012). Cluster analysis of global lower mantle tomography: A new class of structure and implications for chemical heterogeneity. *Earth and Planetary Science Letters*, *357-358*, 68–77. https://doi.org/10.1016/j.epsl.2012.09.014

Lemnifi, A. A., Liu, K. H., Gao, S. S., Reed, C. A., Elsheikh, A. A., Yu, Y., & Elmelade, A. A. (2015). Azimuthal anisotropy beneath north central Africa from shear wave splitting analyses. *Geochemistry, Geophysics, Geosystems*, *16*, 1105–1114. https://doi.org/10.1002/2014GC005706

Li, M., McNamara, A. K., & Garnero, E. (2014). Chemical complexity of hotspots caused by cycling oceanic crust through mantle reservoirs. *Nature Geoscience*, *7*, 366–370. https://doi.org/10.1038/NGEO2120

Lin, Y. P., Zhao, L., & Hung, S. H. (2014). Full-wave effects on shear wave splitting. *Geophysical Research Letters*, *41*, 799–804. https://doi.org/10.1002/2013GL058742

Lithgow-Bertelloni, C., & Richards, M. A. (1998). The dynamics of Cenozoic and Mesozoicplate motions. *Reviews of Geophysics*, *36*, 27–78. https://doi.org/10.1029/97RG02282

Long, M. D. (2009). Complex anisotropy in D″ beneath the eastern Pacific from SKS–SKKS splitting discrepancies. *Earth and Planetary Science Letters*, *283*(1–4), 181–189. https://doi.org/10.1016/j.epsl.2009.04.019

Long, M. D., & Lynner, C. (2015). Seismic anisotropy in the lowermost mantle near the Perm Anomaly. *Geophysical Research Letters*, *42*, 7073–7080. https://doi.org/10.1002/2015GL065506

Long, M. D., & Silver, P. G. (2009). Shear wave splitting and mantle anisotropy: Measurements, interpretations, and new directions. *Surveys in Geophysics*, *30*(4-5), 407–461. https://doi.org/10.1007/s10712-009-9075-1

Lynner, C., & Long, M. D. (2012). Evaluating contributions to SK(K)S splitting from lower mantle anisotropy: A case study from station DBIC, Côte D'Ivoire. *Bulletin of the Seismological Society of America*, *102*(3), 1030–1040. https://doi.org/10.1785/0120110255

Lynner, C., & Long, M. D. (2014). Lowermost mantle anisotropy and deformation along the boundary of the African LLSVP. *Geophysical Research Letters*, *41*, 3447–3454. https://doi.org/10.1002/2014GL059875

McNamara, A. K., Karato, S., & van Keken, P. E. (2001). Localization of dislocation creep in the lower mantle: Implications for the origin of seismic anisotropy. *Earth and Planetary Science Letters*, *191*(1-2), 85–99. https://doi.org/10.1016/S0012-821X(01)00405-8

McNamara, A. K., van Keken, P. E., & Karato, S. (2002). Development of anisotropic structure by solid-state convection in the Earth's lower mantle. *Nature*, *416*(6878), 310–314. https://doi.org/10.1038/416310a

McNamara, A. K., & Zhong, S. (2005). Thermochemical structures beneath Africa and the Pacific Ocean. *Nature*, *437*(7062), 1136–1139. https://doi.org/10.1038/nature04066

Meade, C., Silver, P. G., & Kaneshima, S. (1995). Laboratory and seismological observations of lower mantle isotropy. *Geophysical Research Letters*, *22*(10), 1293–1296. https://doi.org/10.1029/95GL01091

Miyagi, L., Kanitpanyacharoen, W., Kaercher, P., Lee, K. K. M., & Wenk, H. R. (2010). Slip systems in $MgSiO_3$ post-perovskite: Implications for D′′ anisotropy. *Science*, *329*(5999), 1639–1641. https://doi.org/10.1126/science.1192465

Monteiller, V., & Chevrot, S. (2010). How to make robust splitting measurements for single-station analysis and three-dimensional imaging of seismic anisotropy. *Geophysical Journal International*, *182*, 311–328. https://doi.org/10.1111/j.1365-246X.2010.04608.x

Montelli, R., Nolet, G., Dahlen, F. A., Masters, G., Engdahl, R., & Hung, S.-H. (2004). Finite frequency tomography reveals a variety of plumes in the mantle. *Science*, *303*(5656), 338–343. https://doi.org/10.1126/science.1092485

Morgan, W. J. (1971). Convection plumes in the lower mantle. *Nature*, *230*(5288), 42–43. https://doi.org/10.1038/230042a0

Mulyukova, E., Steinberger, B., Dabrowski, M., & Sobolev, S. V. (2015). Survival of LLSVPs for billions of years in a vigorously convecting mantle: Replenishment and destruction of chemical anomaly. *Journal of Geophysical Research: Solid Earth*, *120*, 3824–3847. https://doi.org/10.1002/2014JB011688

Ni, S., & Helmberger, D. V. (2001). Probing an ultra-low velocity zone at the core mantle boundary with *P* and *S* waves. *Geophysical Research Letters*, *28*(12), 2345–2348. https://doi.org/10.1029/2000GL012766

Ni, S., Tan, E., Gurnis, M., & Helmberger, D. (2002). Sharp sides to the African superplume. *Science*, *296*(5574), 1850–1852. https://doi.org/10.1126/science.1070698

Niu, F., & Perez, A. M. (2004). Seismic anisotropy in the lower mantle: A comparison of waveform splitting of SKS and SKKS. *Geophysical Research Letters*, *31*, L24612. https://doi.org/10.1029/2004GL021196

Nowacki, A., Wookey, J., & Kendall, J. M. (2011). New advances in using seismic anisotropy, mineral physics and geodynamics to understand deformation in the lowermost mantle. *Journal of Geodynamics*, *52*(3-4), 205–228. https://doi.org/10.1016/j.jog.2011.04.003

Reiss, M. C., & Rümpker, G. (2017). SplitRacer: MATLAB code and GUI for semiautomated analysis and interpretation of teleseismic shear-wave splitting. *Seismological Research Letters*, *88*, 392. https://doi.org/10.1785/0220160191

Reiss, M. C., Rümpker, G., Tilmann, F., Yuan, X., Giese, J., & Rindraharisaona, E. J. (2016). Seismic anisotropy of the lithosphere and asthenosphere beneath southern Madagascar from teleseismic shear wave splitting analysis and waveform modeling. *Journal of Geophysical Research: Solid Earth*, *121*, 6627–6643. https://doi.org/10.1002/2016JB013020

Restivo, A., & Helffrich, G. (2006). Core–mantle boundary structure investigated using *SKS* and *SKKS* polarization anomalies. *Geophysical Journal International*, *165*(1), 288–302. https://doi.org/10.1111/j.1365-246X.2006.02901.x

Ritsema, J., Deuss, A., van Heijst, H. J., & Woodhouse, J. H. (2011). S40RTS: A degree-40 shear-velocity model for the mantle from new Rayleigh wave dispersion, teleseismic traveltime and normal-mode splitting function measurements. *Geophysical Journal International*, *184*(3), 1223–1236. https://doi.org/10.1111/j.1365-246X.2010.04884.x

Rümpker, G., & Ryberg, T. (2000). New "Fresnel-zone" estimates for shear-wave splitting observations from finite-difference modeling. *Geophysical Research Letters*, *27*(13), 2005–2008. https://doi.org/10.1029/2000GL011423

Savage, M. K. (1999). Seismic anisotropy and mantle deformation: What have we learned from shear wave splitting? *Reviwes Geophysics*, *37*(1), 65–106. https://doi.org/10.1029/98RG02075

Silver, P. G., & Chan, W. W. (1991). Shear wave splitting and subcontinental mantle deformation. *Journal of Geophysical Research*, *96*(B10), 16,429–16,454. https://doi.org/10.1029/91JB00899

Silver, P. G., & Long, M. D. (2011). The non-commutivity of shear wave splitting operators at low frequencies and implications for anisotropy tomography. *Geophysical Journal International*, *184*(3), 1415–1427. https://doi.org/10.1111/j.1365-246X.2010.04927.x

Steinberger, B., & Torsvik, T. H. (2012). A geodynamic model of plumes from the mar-gins of Large Low Shear Velocity Provinces. *Geochemistry, Geophysics, Geosystems*, *13*, Q01W09. https://doi.org/10.1029/2011GC003808

Tandon, G. P., & Wenig, G. J. (1984). The effect of aspect ratio of inclusions on the elastic properties of unidirectionally aligned composites. *Polymer Composites*, *5*(4), 327–333. https://doi.org/10.1002/pc.750050413

Teanby, N., Kendall, J., & van der Baan, M. (2004). Automation of shear-wave splitting measurements using cluster analysis. *Bulletin of the Seismological Society of America*, *94*(2), 453–463. https://doi.org/10.1785/0120030123

Tepp, G., Ebinger, C. J., Zal, H., Gallacher, R., Accardo, N., Shillington, D. J., et al. (2018). Seismic anisotropy of the upper mantle below the Western rift, East Africa. *Journal of Geophysical Research: Solid Earth*, *123*(7), 5644–5660. https://doi.org/10.1029/2017JB015409

Tommasi, A., Goryaeva, A., Carrez, P., Cordier, P., & Mainprice, D. (2018). Deformation, crystal preferred orientations, and seismic anisotropy in the Earth's D″ layer. *Earth and Planetary Science Letters*, *492*, 35–46. https://doi.org/10.1016/j.epsl.2018.03.032

Walker, A. M., Forte, A. M., Wookey, J., Nowacki, A., & Kendall, J. M. (2011). Elastic anisotropy of D″ predicted from global models of mantle flow. *Geochemistry, Geophysics, Geosystems*, *12*, Q10006. https://doi.org/10.1029/2011GC003732

Walker, A. M., & Wookey, J. (2012). MSAT—A new toolkit for the analysis of elastic and seismic anisotropy. *Computers & Geosciences*, *49*, 81–90. https://doi.org/10.1016/j.cageo.2012.05.031

Walsh, E., Arnold, R., & Savage, M. K. (2013). Silver and Chan revisited. *Journal of Geophysical Research: Solid Earth*, *118*, 5500–5515. https://doi.org/10.1002/jgrb.50386

Wang, Y., & Wen, L. (2004). Mapping the geometry and geographic distribution of a very low velocity province at the base of the Earth's mantle. *Journal of Geophysical Research*, *109*(B10), B10305. https://doi.org/10.1029/2003JB002674

Wang, Y., & Wen, L. (2007). Complex seismic anisotropy at the border of a very low velocity province at the base of the Earth's mantle. *Journal of Geophysical Research*, *112*(B9), B09305. https://doi.org/10.1029/2006JB004719

Wen, L. (2001). Seismic evidence for a rapidly varying compositional anomaly at the base of the Earth's mantle beneath the Indian Ocean. *Earth and Planetary Science Letters*, *194*(1-2), 83–95. https://doi.org/10.1016/S0012-821X(01)00550-7

Wentzcovitch, R. M., Tsuchiya, T., & Tsuchiya, J. (2006). $MgSiO_3$ postperovskite at D″ conditions. *Proceedings of the National Academy of Science*, *103*(3), 543–546. https://doi.org/10.1073/pnas.0506879103

Wicks, J. K., Jackson, J. M., & Sturhahn, W. (2010). Very low sound velocities in iron-rich (Mg, Fe)O: Implications for the core–mantle boundary region. *Geophysical Research Letters*, *37*, L15304. https://doi.org/10.1029/2010GL043689

Yamazaki, D., & Karato, S. (2013). Lattice-preferred orientation of lower mantle materials and seismic anisotropy in the D″ layer. In K. Hirose, et al. (Eds.), *Post-perovskite: The last mantle phase transition*, *American Geophysical Union Geophysical Monograph Series*, (Vol. 174, pp. 69–78). https://doi.org/10.1029/174GM07

Yu, S., & Garnero, E. J. (2018). Ultra-low velocity zone locations: A global assessment. *Geochemistry, Geophysics, Geosystems*, *19*(2), 396–414. https://doi.org/10.1002/2017GC007281